Ocean redox structure across the Late Neoproterozoic Oxygenation Event: A nitrogen isotope perspective

Magali P Ader, Pierre P Sansjofre, Galen P Halverson, Vincent P Busigny, Ricardo I. F. Trindade, Marcus P Kunzmann, Afonso C. R. Nogueira

Ocean redox structure across the Late Neoproterozoic Oxygenation Event: A nitrogen isotope perspective

Magali Ader[a,*], Pierre Sansjofre[a,b,c], Galen P. Halverson[d], Vincent Busigny[a], Ricardo I.F. Trindade[c], Marcus Kunzmann[d], Afonso C.R. Nogueira[e]

[a] Institut de Physique du Globe de Paris, Sorbonne Paris Cité, University Paris Diderot, UMR 7154 CNRS, 1 rue Jussieu, 75238 Paris, France

[b] Departamento de Geofísica, Instituto de Astronomia, Geofísica e Ciências Atmosféricas, Universidade de São Paulo, Rua do Matão 1226, 05508-900 São Paulo, Brazil

[c] now at Laboratoire Domaines Océaniques, Université de Bretagne Occidentale, UMR 6538, 29820 Plouzané, France

[d] Department of Earth and Planetary Sciences/Geotop, McGill University, 3450 University Street, Montréal, QC, Canada H3A 0E8.

[e] Faculdade de Geologia, Instituto de Geociências, Universidade Federal do Pará, CEP 66.075-110, Belém, Brazil.

*Corresponding author:
Magali Ader
Équipe de géochimie des isotopes stables, Institut de Physique du Globe de Paris, 1 rue Jussieu, 75238 Paris, France.
Phone number: +33 (0)1 83 95 75 06
e-mail address: ader@ipgp.fr

Keywords: Nitrogen isotopes, Neoproterozoic, ocean oxygenation, nitrogen biogeochemical cycle, paleoceanography.

Abstract

The end of the Neoproterozoic Era (1000 to 541 Ma) is widely believed to have seen the transition from a dominantly anoxic to an oxygenated deep ocean. This purported redox transition appears to be closely linked temporally with metazoan radiation and extraordinary perturbations to the global carbon cycle. However, the geochemical record of this transition is not straightforward, and individual data sets have been variably interpreted to indicate full oxygenation by the early Ediacaran Period (635 to 541 Ma) and deep ocean anoxia persevering as late as the early Cambrian. Because any change in marine redox structure would have profoundly impacted nitrogen nutrient cycling in the global ocean, the N isotope signature of sedimentary rocks ($\delta^{15}N_{sed}$) should reflect the Neoproterozoic deep-ocean redox transition. We present new N isotope data from Amazonia, northwest Canada, northeast Svalbard, and South China that span the Cryogenian glaciations (~750 to 580 Ma). These and previously published data reveal a N-isotope distribution that closely resembles modern marine sediments, with a mode in $\delta^{15}N$ close to 4‰ and range from -4 and +11‰. No apparent change is seen between the Cryogenian and Ediacarian. Data from earlier Proterozoic samples show a similar distribution, but shifted slightly towards more negative $\delta^{15}N$ values and with a wider range. The most parsimonious explanation for the similarity of these N-isotope distribution is that as in the modern ocean, nitrate (and hence O_2) was stable in most of the middle–late Neoproterozoic ocean, and possibly much of Proterozoic Eon. However, nitrate would likely have been depleted in partially restricted basins and oxygen minimum zones (OMZs), which may have been more widespread than in the modern ocean.

1. Introduction

It is widely argued that the appearance of animals in the geological record is linked to a major step in the oxygenation of Earth's surface environment, known as the Neoproterozoic Oxygenation Event (NOE) (Canfield et al., 2007, 2008; Och and Shields-Zhou, 2012; Scott et al., 2008). The NOE is more difficult to document in the geological record than its early Paleoproterozoic counterpart, the Great Oxidation Event (GOE), whose onset is well established based on the sedimentary record of redox-sensitive detrital minerals and mass independent fractionation of sulfur isotopes (e.g. Farquhar et al., 2000; Lyons et al., 2014). Although the NOE has not been formally defined, one criterion is the timing of ventilation of the deep ocean with sufficient dissolved oxygen to accommodate the earliest animals (Och and Shields-Zhou, 2012). Whereas the cause-and-effect relationship between oxygenation and animal evolution and the oxygen threshold required for early animals are still debated (e.g., Butterfield, 2009; Sperling et al., 2013), eukaryotic diversification and the oxygenation of the environment must have been closely coupled through a complex network of biogeochemical feedbacks linked through the origin, export, decay and burial of organic matter (Butterfield, 2009; Close et al., 2011; Logan et al., 1995; Pawlowska et al., 2013).

Iron speciation data from Neoproterozoic mudstones suggest a transition from dominantly anoxic and ferruginous deep oceans with prevalent sulfidic (euxinic) conditions in continental margin settings (Planavsky et al., 2011; Poulton and Canfield, 2011) to dominantly anoxic and ferruginous deep oceans with only occasional evidence for euxinic conditions in the early–middle Neoproterozoic (Canfield et al., 2008), followed by deep-ocean ventilation in the late Ediacaran (Canfield et al., 2007). However, these data only provide information about local depositional redox conditions and do not bear directly on the state of the deep ocean. Trace metal

abundances (Mo, U, V, and Cr) in euxinic sediments, although sensitive to local conditions, are also strongly dependent on the volume of oxygenated water masses, hence they bear on global redox conditions in the oceans (Algeo and Rowe, 2012). A series of separate studies and compilations of trace metal data have been published recently. All show a dramatic increase in abundances in the Ediacaran first interpreted to record deep ocean ventilation (635–541 Ma; Scott et al., 2008; Och and Shields-Zhou, 2012; Sahoo et al., 2012; Partin et al., 2013), broadly consistent with iron speciation data. Yet, data from some individual basins variably indicate persistently anoxic (Li et al., 2010; Johnston et al., 2013) versus oxygenated (Johnston et al., 2012; Sansjofre et al., 2014) bottom-waters throughout most of the Ediacaran Period. Other data imply widespread oxygen-deficient conditions in the earliest Cambrian (e.g. Schroder and Grotzinger, 2007; Cremonese et al., 2013) despite the appearance of complexly burrowing bilaterians. An emerging model is that anoxic conditions on continental platforms was locally controlled (Kah and Bartley, 2011; Shen et al., 2011), the deep ocean being pervasively oxygenated, but with a low oxygen concentration preventing the stabilization of oxic conditions in platforms throughout the Ediacaran Period (Johnston et al., 2012, 2013). Recent modeling coupled with trace metal compilations further suggests that no more than 40% of the pre-NOE seafloor could have been anoxic and no more than 10% euxinic (Partin et al., 2013; Reinhard et al., 2013). These models and existing data thus allow for the possibility that much of the global ocean may have been oxygenated prior to the Ediacaran Period.

We have applied the nitrogen isotope system to the question of the NOE because the N-isotopic composition of marine sediments ($\delta^{15}N_{sed}$; where the standard delta notation and normalization to atmospheric N_2 is used; Mariotti et al., 1981) is strongly dependent on the nitrogen biogeochemical cycle in the water column, itself controlled by the ocean redox structure (Boyle

et al., 2013; Canfield et al., 2010; Fennel et al., 2005; Quan and Falkowski, 2009). Although the present day nitrogen cycle is highly complex and remains poorly understood in detail (e.g. Lam et al., 2011; Sigman et al., 2009a), the current understanding of its basic features and of its isotopic imprint in the sedimentary record (Galbraith et al., 2008; Sigman et al., 2009b) have already motivated the application of $\delta^{15}N_{sed}$ to elucidate nitrogen biogeochemical cycling in past oceans. Nitrogen isotopes have been applied to the Phanerozoic (e.g. Algeo et al., 2008; Higgins et al., 2012; Junium and Arthur, 2007; Quan et al., 2008) and Precambrian records (Beaumont and Robert, 1999; Busigny et al., 2013; Garvin et al., 2009; Godfrey and Falkowski, 2009; Godfrey et al., 2013; Kump et al., 2011; Papineau et al., 2009, 2013; Stüeken, 2013; Thomazo et al., 2009, 2011) as a proxy for both ocean redox and nitrogen biogeochemistry. Here we add a new nitrogen isotope dataset from ~750 to 580 Ma strata from multiple cratons to a growing Neoproterozoic database of both bulk sedimentary ($\delta^{15}N_{sed}$) and kerogen ($\delta^{15}N_{ker}$) nitrogen isotope data (Cremonese et al., 2013; Kikumoto et al., 2014; Spangenberg et al., 2014) to test whether the NOE is recorded in nitrogen isotope signatures. These results show that the $\delta^{15}N_{sed}$ distributions for the Cryogenian and the Ediacaran resemble one another and that documented in the modern ocean.

1.1. Isotope Biogeochemistry of the Nitrogen Oceanic Cycle

Nitrogen-isotopic compositions of nitrate, particulate organic matter and surface sediments have been extensively studied to characterize the nitrogen cycle in present oceans and its transcription into the sedimentary record (Fig. 1a, e.g. Robinson et al., 2012; Somes et al., 2010; Tesdal et al., 2013; Thunell et al., 2004). Below we summarize the basic processes and pathways and associated isotope fractionation (expressed using the enrichment factor notation in ‰, $\varepsilon_{a\text{-}b} \approx \delta^{15}N_a - \delta^{15}N_b$) in the oceanic nitrogen cycle.

The initial source of all bioavailable-N to the oceans is the fixation of atmospheric N_2 (N_2-fixation) by aerobic or anaerobic autotrophs, such as cyanobacteria, which transform molecular N_2 into organic matter (via NH_4^+) with a small isotope fractionation ($\varepsilon_{org\text{-}N2}$ ~ -4 to 0‰; e.g. Zerkle et al., 2008). Other primary photosynthetic organisms assimilate remineralized forms of nitrogen mostly as NO_3^- or NH_4^+. The mineralization of organic matter produces NH_4^+ (ammonification) with no net isotope fractionation owing to its efficiency (Möbius, 2013). If NH_4^+ remains stable it can then be assimilated with an isotope effect that increases strongly with its availability ($\varepsilon_{org\text{-}NH4}$ ~ 0‰ to -27‰) such that the organic matter can be markedly ^{15}N-depleted where NH_4^+ is abundant (Pennock et al., 1996). The NH_4^+ may also be oxidized. If this oxidation is not complete, the residual NH_4^+ will be enriched in ^{15}N, because the first oxidation step to nitrite (NO_2^-) involves a strong fractionation ($\varepsilon_{NO2\text{-}NH4}$ ~ -41‰ to -13‰; Casciotti et al., 2003; Mariotti et al., 1981; Santoro and Casciotti, 2011). In oxic environments, this oxidation is accomplished by nitrification (i.e. sequential oxidation to NO_2^- and NO_3^-) and goes to completion, unless ammonium is concurrently assimilated as a nutrient. Subsequent NO_3^- assimilation entails fractionation with $\varepsilon_{org\text{-}NO3\text{-}}$ between 0 and -8‰ in NO_3^--limited and NO_3^--replete conditions, respectively (Pennock et al., 1996; Somes et al., 2010). Under dysoxic conditions (i.e. typically in OMZs or within redox transition zones), NO_3^- as well as available NH_4^+ and NO_2^- are converted into gaseous species (NO_2 and/or N_2) by an incompletely understood combination of metabolic pathways that include heterotrophic denitrification and anammox (anaerobic oxidation of NH_4^+ by NO_2^-), nitrification, nitrate reduction to NH_4^+, chemolithotrophic sulfide-dependent denitrification, co-oxidation of methane and ammonium, and most probably other metabolisms yet to be indentified (Lam et al., 2009, 2011; Lavik et al., 2009; Mandernack et al., 2009; Wenk et al., 2013). In present day OMZs where nitrate

consumption does not reach completion, the net result of these processes is a pronounced ^{15}N-enrichment in the residual NO_3^- pool (Voss et al., 2001) similar to that of the experimentally determined for heterotrophic denitrification ($\varepsilon_{NO3-\ N2}$ ~ +15 to +30‰) (Granger et al., 2008; Mariotti et al., 1981). When NO_3^- consumption proceeds to completion, as in anoxic porewaters, hardly any isotope effect is expressed (Lehmann et al., 2007). Finally, within stable redox transition zones, nitrate (from above) and ammonium (from below) are also near-quantitatively converted into N_2 or N_2O resulting in a discrete zone of ^{15}N-enrichment in nitrate and ammonium (ε_{NO3-N2} ~ +10 ‰; ε_{NH4-N2} ~ +10 ‰) tied to decreasing concentrations (Fuchsman et al., 2008; Thunell et al., 2004; Wenk et al., 2014).

The ocean's redox structure thus tightly controls the nitrogen cycle through the complex network of metabolic pathways by which nitrogen flows between reservoirs. The local redox conditions determine the dissolved inorganic nitrogen speciation, nitrate being stable in oxic waters and ammonium in anoxic waters. The nature (i.e. OMZs versus redox transition zones), location (shallow versus deep), and spatial extent of dysoxic zones determine the rate of nitrate and ammonium conversion to N_2 or N_2O, as well as their ^{15}N enrichment.

1.2. Expected $\delta^{15}N_{sed}$ signature under different ocean redox structures

On continental margins and in anoxic basins, $\delta^{15}N_{sed}$ mostly records the isotopic composition of primary producers, with only minor modification of (e.g. Robinson et al., 2012; Tesdal et al., 2013; Thunell et al., 2004). The $\delta^{15}N$ of the primary producers depends on the mass and isotope balance between the two main sources of nitrogen supporting the new primary productivity, i.e. N_2-fixation and upwelled nitrate and/or ammonium reaching the photic zone (e.g. Somes et al., 2010). Because both this balance and the nitrate isotope composition are ultimately linked to the

redox structure of the global ocean, $\delta^{15}N_{sed}$ should reflect this redox structure, even though its isotopic signature is acquired in surface waters.

We review conceptual scenarios for the nitrogen cycle and $\delta^{15}N_{sed}$ expression based on two ocean redox structures envisaged for the Neoproterozoic: a dominantly oxygenated ocean and a redox-stratified ocean. In a dominantly oxygenated ocean (Fig. 1a), nitrate is the main form of bioavailable nitrogen and it is generated by nitrification of the ammonium released by remineralized organic matter. In the surface mixed layer, which broadly corresponds to the euphotic zone, ammonium and nitrate are usually quantitatively reassimilated to support primary productivity, without net isotope fractionation. Deeper, regenerated nitrate accumulates and eventually returns to the surface ocean in upwelling zones. When the upwelling passes through dysoxic or anoxic OMZs, a fraction of this nitrate pool is denitrified, increasing the $\delta^{15}N$ of residual nitrate ultimately delivered to the surface. The nitrogen isotope composition of nitrate ($\delta^{15}N_{NO3-}$) in surface waters can thus strongly vary regionally (between +1 and +15‰) depending on ocean circulation patterns and on deep and intermediate water redox condition (Somes et al., 2010). The $\delta^{15}N_{sed}$ distribution of present-day ocean surface sediments captures this range of variation, with a mode at 5–6‰ (Fig. 2a; Tesdal et al., 2013), a small negative tail approaching 1‰ and a large positive tail to +15‰ corresponding to OMZs.

In a redox-stratified ocean (Fig 1b and c), the inorganic nitrogen generated by organic matter mineralization will be in the form of nitrate above the redox transition zone and ammonium below. The redox transition is unlikely to be stable in the surface mixed layer, owing to its rapid mixing time. Thus in most locations the redox transition zone should stabilize below the surface mixed layer, except possibly in up-welling zone where it may reach the surface (Kump et al., 2005)(Fig. 1c). In a stable situation, nitrate is depleted by assimilation in the surface mixed layer

and accumulates below until it reaches the redox transition zone, where it is denitrified. Below the redox transition zone, ammonium accumulates. In this configuration, ammonium does not reach the surface. It is quantitatively converted to N_2 or N_2O within the redox transition zone by coupled nitrification–heterotrophic denitrification and anammox, as observed today in the Cariaco basin and the Black sea (Fuchsman et al., 2008; Meckler et al., 2007; Thunell et al., 2004). Overall this scenario results in extensive loss of bioavailable nitrogen (nitrate and ammonium) compared to the oxic ocean scenario. Only nitrate accumulated in between the surface mixed layer and the redox transition zone may ultimately remix into the surface ocean in upwelling zones (Fig. 1b). But this accumulation is strongly limited by down-welling zones where denitrification will occur as the nitrate crosses the redox transition zone. The amount of nitrate available for recharging the surface ocean is thus strongly controlled by the depth of the redox transition zone. The closer the redox transition zone is to the base of the surface mixed layer, the smaller the nitrate reservoir is. Resulting nitrate limitation is compensated by N_2-fixation, which drives surface nitrate $\delta^{15}N$ towards 0‰ (Quan and Falkowski, 2009), as observed in Mediterranean sapropels and sedimentary rocks deposited during ocean anoxic events (OAEs; Fig. 2b and references therein). Locally, upwelling currents may be vigorous enough for some of the ammonium to traverse the redox transition zone before being fully converted to N_2 or N_2O. In this case, the ^{15}N-enriched residual ammonium will be assimilated either directly or after having been oxidized to nitrate, producing positive $\delta^{15}N_{sed}$ signatures similar to those found in present-day OMZs (Fig. 1b). This process has recently been proposed to explain positive $\delta^{15}N$ values on a late Paleoproterozoic platform (Godfrey et al., 2013). If the redox transition zone was shallow enough (Fig. 1c), it may impinge on the surface mixed layer in upwelling zones possibly reaching the surface (Kump et al., 2005). In this case, ammonium would be competitively

assimilated by primary producers and converted to N_2 or N_2O by coupled nitrification–heterotrophic denitrification and anammox. Strong upwelling would favor ammonium assimilation and negative $\delta^{15}N_{sed}$, as has been proposed to explain values as low as -4‰ during OAE2 (Higgins et al., 2012), but where conversion to N_2 or N_2O dominates, $\delta^{15}N_{sed}$ values would trend positive (e.g., Papineau et al., 2009). Given the instability of the redox transition zone in the surface mixed layer, $\delta^{15}N_{sed}$ values should be highly variable both temporally and spatially, as observed in the c.a. 2.0 Ga Lower Aravalli Group (Papineau et al., 2009)(Fig. 2g). The $\delta^{15}N_{sed}$ distribution of a stratified redox scenario should reflect it with high variability, ranging from negative to positive values, and with a mode close to 0‰.

This brief overview highlights the difficulty of predicting $\delta^{15}N_{sed}$ signatures under non-actualistic scenarios. It also demonstrates the difficulty in extrapolating results from a single basin to interpreting the global nitrogen cycle given the intrinsic complexity and heterogeneity of the nitrogen cycle. However, it raises the possibility that distributions of $\delta^{15}N_{sed}$ from several globally distributed locations hold key information on the global nitrogen cycle. Specifically, the $\delta^{15}N_{sed}$ distribution in redox-stratified scenarios are expected to show a mode closer to 0‰ (Quan and Falkowski, 2009) with marked tails toward negative and positive $\delta^{15}N_{sed}$ values in up-welling regions. For this reason we have chosen to integrate data from multiple basins to produce a global picture of $\delta^{15}N_{sed}$ spanning the purported NOE, i.e. from 750 to 580 Ma.

2. Samples

We present new $\delta^{15}N_{sed}$ data from four late Neoproterozoic basins that straddled the equator during the Marinoan glaciation (Fig. 3): (i) the Datangpo and Doushantuo formations sampled from the Yangjiaping section (~720-580 Ma), South China; (ii) the Mirasol d'Oeste and Guia

231 formations sampled from 4 sections spanning a cross-section of the Araras platform, Brazil; (iii)
232 the Elbobreen and Dracoisen formations sampled from a composite section (~750–600 Ma) in
233 northeast Svalbard; (iv) and the Twitya and Sheepbed formations from a composite section
234 (~660–600 Ma) in northwest Canada. Most samples are Ediacaran (635–541 Ma) in age, such
235 that this data set spans the first fossil evidence of bilaterians (~575 Ma; Narbonne and Gehling,
236 2003) and record what is commonly regarded as a transition from dominantly anoxic to
237 oxygenated oceans (Fike et al., 2006; Sahoo et al., 2012). A small subset of older samples
238 extends the record beyond the Cryogenian (c.a. 720–635 Ma) glaciations. A description of
239 geological backgrounds for the sampled sections is included in the supplementary material. We
240 only summarize below the depositional depth and redox conditions inferred for each of these
241 sections.

242 In the Yangtze platform (South China) sections, iron speciation, trace metal contents, sulfur and
243 carbon isotopes, and pyrite morphologies indicate that the water column was redox stratified
244 during the deposition of both the Datangpo and Doushantuo formations (Ader et al., 2009;
245 McFadden et al., 2007; Li et al., 2010; Li et al., 2012; Wang et al., 2012). However, enrichment
246 of Mo in Doushantuo shales indicates that a significant percentage of the open ocean must have
247 been oxygenated at the time (Sahoo et al., 2012). At Yangjiaping, both formations were probably
248 deposited in oxic shallow waters (Ader et al., 2009; Li et al., 2012; Wang et al., 2012), while at
249 the Wuhe section, for which previous $\delta^{15}N_{sed}$ results are available (Kikumoto et al., 2014), the
250 Doushantuo Formation was deposited in a deep anoxic inner-shelf environment.

251 On the Araras platform, the four studied sections span a platform transect (Fig. S1) in an overall
252 deepening upward succession: the lower Mirassol d'Oeste Formation was deposited in shallow
253 water and overlying Guia Formation was deposited in increasingly deeper environments, with

the upper part of the unit deposited in a slope setting. The trace metal contents in the same samples for which $\delta^{15}N_{sed}$ have been obtained indicate a fully oxygenated water column, with possible episodes of porewater anoxia approaching the sediment-water interface on the slope (Sansjofre et al., 2014).

Shales from Svalbard and Canada were all deposited below storm wave base. For the Elbobreen and Dracoisen formations (Northeast Svalbard) Fe/Al data lie close to the local detrital baseline of 0.58 with a few values above but most lying below (Table S1 in supplementary material). These results are not conclusive, but are consistent with liberation of iron from ferrouginous OMZs (Fe/Al < 0.58) and subsequent addition to more oxygenated parts of the water column, as occurs in modern OMZs (Scholz et al., 2014). We have no direct constraints on the depositional redox conditions of our samples from the Twitya and Sheepbed formations (Northwest Canada). However, iron speciation data are available for correlative sections of the lower Sheepbed Formation (Johnston et al., 2013; Shen et al., 2008). These data were interpreted to indicate anoxic and ferruginous deep waters with variations in the redox transition zone depth, such that the depositional environment may have been oxic in some locations. We note, however, that FeHR/FeT data lie close to the 0.38 threshold used to discriminate anoxic from oxic environments and the FeT/Al ratio are close to both the generic detrital ratio of 0.53 (Johnston et al., 2013), which means the data do not conclusively demonstrate anoxic conditions. As for Svalbard, it is possible that ferruginous conditions were confined to an OMZ in an otherwise oxygenated ocean.

3. Nitrogen stable isotope analyses

Samples were ground in an agate mortar and sieved to ensure a grain size <140 µm. To concentrate nitrogen in the insoluble residue, most carbonate-rich samples were first decarbonated in HCl 6 N overnight at room temperature, followed by 2 h at 80°C. Residues were washed with distilled water, centrifuged and dried at 50°C. When enough material was available and N-content was above 200 ppm, samples were prepared by conventional sealed tube combustion to convert total nitrogen to N_2 (Dumas combustion). This method is hereafter referred to as the conventional method (see Ader et al. (1998) for a detailed description). The N_2 was then measured on a dual inlet Thermo Finnigan Delta+XP mass spectrometer allowing analyses on as low as 2 micromoles N_2 with a precision of ± 0.2‰ (1σ). Nitrogen blanks were approximately 0.15 micromole, thus representing less than 10% of the measured nitrogen on the least N-rich samples. The reproducibility of the $\delta^{15}N_{sed}$ measurements was ± 0.2‰ (1σ).

For samples containing a limited amount of material, N-isotope analyses were performed using sealed-tube combustion and on-line N_2 purification on an ultra-high vacuum line with direct introduction to a static mass spectrometer (hereafter referred to as the static method) following an established protocol (Ader et al., 2006; Busigny et al., 2003, 2005; Thomazo et al., 2011). Powdered samples (between 5 and 30 mg) were embedded in a platinum parcel, then evacuated under vacuum at 150°C before being sealed in an evacuated and pre-purified quartz tube with an excess of CuO and Cu wire and CaO granules. The sample was combusted at 950 °C for 6 h and the resulting N_2 purified and quantified on an ultra-high vacuum line directly coupled to our static mass spectrometer. Precision for $\delta^{15}N$ via this method is ± 0.3‰ (1σ) based on repeat analyses. Blanks yielded $\delta^{15}N$ values of +1.5 ± 3‰ and higher nitrogen amounts (~ 30 ng) than expected based on prior work in our lab (Ader et al., 2006; Busigny et al., 2005; Thomazo et al., 2011), which is likely a result of the lower sample degassing temperature set at 150°C to avoid

298 nitrogen devolatilisation, the thermal maturation experienced by our samples being lower than
299 greenschist facies. In most cases this blank content accounts for less than 3% of the total
300 nitrogen, but reached 10% in some of the most nitrogen-poor samples. All results are blank-
301 corrected and given in standard δ notation, calibrated to Air (Mariotti et al., 1981).

302 In order to ascertain whether bulk and decarbonated samples, as well as conventional and static
303 methods, yield comparable results, selected samples were analyzed by multiple methods (Table
304 S2). $\delta^{15}N_{sed}$ results obtained on bulk and decarbonated samples using the conventional or the
305 static method compare well given the reproducibility of each method. When all data are
306 considered together, the $\delta^{15}N_{sed}$ reproducibility (1σ) is usually better than ±0.35‰, and always
307 better than ±0.63‰. N-contents also compare quite well between methods, except for pure
308 carbonate samples, for which bulk N-contents measured on the decarbonated residue are often
309 lower than those measured directly on bulk samples. It is likely that a significant fraction of the
310 very small residue was lost during the decarbonation step, probably as a supernatant during
311 rinsing and centrifugation. Therefore, N-contents determined using the decarbonated residue of
312 carbonate samples are probably slightly underestimated.

313 **4. Results**

314 Our $\delta^{15}N_{sed}$ results are listed in the supplementary information Table S3 and presented as
315 chemostratigraphic profiles (together with available $\delta^{13}C_{org}$ and $\delta^{13}C_{carb}$ data) for each of the
316 studied sections in Figure 4. For the Araras platform (n=41), $\delta^{15}N_{sed}$ data have been obtained
317 from 4 sections spanning the platform (Fig. 4a-c). $\delta^{15}N_{sed}$ data for the shallow-water cap
318 dolostone of the Mirassol d'Oeste Formation (directly overlying the Marinoan glacial deposits)
319 are only available in the Terconi-Camil composite section. They show the largest distribution

320 with $\delta^{15}N_{sed}$ values ranging from +2 to +10‰ (Fig. 4a). $\delta^{15}N_{sed}$ data for the overlying Guia
321 Formation are available for all three sections (Fig. 4a-c). They lie between +2 and +6‰, and no
322 systematic variation is apparent either temporally or between sections.

323 For South China, all samples come from the Yangjkiaping section (Fig. 4d). In the Datangpo
324 Formation, $\delta^{15}N_{sed}$ data cluster around +4‰. In the Doushantuo Formation, $\delta^{15}N_{sed}$ values
325 increase within the 4 meter-thick cap carbonate from +3‰ up to +5.5‰, at which they remain
326 through the subsequent 40 m. Above, $\delta^{15}N_{sed}$ values are more variable, but overall decrease to
327 +2.5‰ in the lower Dengying Formation. Recently published $\delta^{15}N_{sed}$ data from the Doushantuo
328 Formation from a drill-core in the Three Gorges area that penetrates a deep inner-shelf setting on
329 the Yangtze platform (Kikumoto et al., 2014) show similar $\delta^{15}N_{sed}$ values than the Yangjiaping
330 section, which correspond to the shelf margin (Fig. 2c). Both sections also display similar $\delta^{15}N_{sed}$
331 stratigraphic variations (Fig. 4d, this study and Fig. 2, Kikumoto et al., 2014) in spite of the
332 different depositional setting, lithologies and $\delta^{13}C_{org}$ and $\delta^{13}C_{carb}$ stratigraphic variations.
333 Samples from Svalbard (n=18) present very homogeneous $\delta^{15}N_{sed}$ values ranging from +4.1 to
334 +6.3‰ (Fig. 4e), although data from the post-Marinoan Dracoisen Formation show a distinct
335 positive upward trend from +4 to +5.5‰ (Fig. 4e). All samples from northwest Canada (n=8)
336 fall between +2 and 4‰ (Fig. 4f). No obvious correlation with $\delta^{13}C_{org}$ and $\delta^{13}C_{carb}$ is evident in
337 any of the sections (Fig. 4 and Fig. 5d).

338 These results are synthesized in histograms in Figure 2 together with $\delta^{15}N_{sed}$ data previously
339 published for the Doushantuo and Dengying formations, South China (Cremonese et al., 2013;)
340 and $\delta^{15}N_{kerogen}$ data from the Tamengo Formation, Brazil (Kikumoto et al., 2014; Spangenberg et
341 al., 2014). $\delta^{15}N_{sed}$ values for South China range between +2.2 and +8.5‰ (Fig. 2c); for the
342 Amazonian craton between +2.2 and +10.5‰; for the Late Ediacaran Tamengo Formation

between -3.3 and +3.1‰, defining the lower end of the distribution (Fig. 2d); for northwestern Canada between +2 and +4‰ and for Svalbard between +4 and +7‰ (Fig. 2e). Overall, the $\delta^{15}N$ values (n = 158) range from -3.3 to +10.5‰, with roughly 40% of the data falling between +3 and +6‰ (Fig. 2f). No time-based evolution is evident from the comparison of the Cryogenian values to those of the Ediacaran (Fig. 2f).

5. Discussion

5.1. Preservation of the $\delta^{15}N_{sed}$ signature

In sediments from continental margins and anoxic depositional settings, $\delta^{15}N$ of primary producers is recorded with only minor modification in $\delta^{15}N_{sed}$ in spite of the early diagenetic remineralization of organic matter and ammonium fixation in clay minerals (e.g. reviews in Robinson et al., 2012; Thomazo et al., 2011). The conservation of primary signatures is illustrated in sediments from the eastern Mediterranean sapropels and the OAE2 event in the proto-North Atlantic by the similarity between $\delta^{15}N_{sed}$, $\delta^{15}N_{kerogen}$ and $\delta^{15}N$ of primary producers as reconstructed from porphyrin $\delta^{15}N$ (Higgins et al., 2010; 2012). However, most Precambrian sedimentary rocks have experienced some degree of post-depositional $\delta^{15}N_{sed}$ modification. Devolatilization of fixed ammonium during metamorphism has been identified as the main culprit. At metamorphic grades higher than greenschist facies, a decrease in N content is often coupled to an increase in $\delta^{15}N_{sed}$ as ^{15}N-depleted fixed ammonium is preferentially volatilized (Bebout and Fogel, 1992; Busigny et al., 2003; Jia and Kerrich 2004; Jia, 2006; Mingram and Brauer 2001; Pinti et al., 2009; Yui et al., 2009). The reliability of $\delta^{15}N_{sed}$ in Precambrian sedimentary rocks as a tracer for initial $\delta^{15}N$ of primary producers thus remains controversial. This problem has been addressed by comparing $\delta^{15}N_{sed}$ and $\delta^{15}N_{kerogen}$ data from the same

successions (Godfrey et al., 2009, 2013; Kump et al., 2011), on the basis that $\delta^{15}N_{kerogen}$ should not be modified by metamorphism (Ader et al., 1998, 2006; Boudou et al., 2008). So far, these comparisons have shown mixed results: two successions show $\delta^{15}N_{sed}$ to be higher than $\delta^{15}N_{kerogen}$ by up to +6‰ (Kump et al., 2011) and +12‰ (Godfrey et al., 2013), whereas others successions yield comparable $\delta^{15}N_{sed}$ and $\delta^{15}N_{kerogen}$ values (Godfrey et al., 2009, 2013). The two successions with higher $\delta^{15}N_{sed}$ than $\delta^{15}N_{kerogen}$ are recognized as having undergone lower greenschist facies (Kump et al., 2011) or higher (Godfrey et al., 2013) peak metamorphic conditions. Peak metamorphic temperatures for the other successions are not reported. These mixed results raise the specter of overprinting of $\delta^{15}N_{sed}$ by devolatilization and/or of overprinting of $\delta^{15}N_{kerogen}$ by N-contamination during the HF extraction of N-poor kerogen (Ader et al., 2006) in rocks metamorphosed to greenschist or higher facies. They nevertheless suggest that $\delta^{15}N_{sed}$ may be preserved in rocks that have experienced minimal metamorphism.

In any case, for this study the maximum metamorphic conditions for the studied locations were below greenschist facies (Supplementary material), minimizing the risk of post-depositional modification of the $\delta^{15}N_{sed}$ signal. N/C ratios strongly vary (Fig. 5b), but the N and TOC contents of decarbonated samples show a rough correlation (Fig. 5c), suggesting N originates from the organic carbon matter. The fact that $\delta^{15}N_{sed}$ does not correlate with either N_{decarb} content (Fig. 5a) or C/N ratio (Fig. 5b) suggests that even if some nitrogen was redistributed between organic matter, clay minerals and fluid phases during diagenesis and low-grade metamorphism, bulk $\delta^{15}N_{sed}$ values should not have been significantly modified. Finally, it would be very unlikely for burial and metamorphic processes to have resulted in the observed similarities in $\delta^{15}N_{sed}$ values across all studied locations, as well as across transects of the Araras and Yangtze platforms, in

spite of the variable lithologies and thermal histories. We thus proceed on the assumption that $\delta^{15}N_{sed}$ values reflect primary biomass signatures.

5.2 Significance of $\delta^{15}N_{sed}$ in the context of global ocean redox structure

The distribution of $\delta^{15}N_{sed}$ in analyzed Neoproterozoic rocks (mode of ~ +4‰, Fig. 2c) is clearly more like that of modern sediments (mode of ~ +5‰, Fig. 2a) than to that of OAEs (mode of ~ -1‰, Fig. 2b). The fact that most $\delta^{15}N_{sed}$ values do not cluster in the -4 to + 2‰ range typical of OAEs, which have been consistently interpreted as representing episodes of redox stratification, indicates that during most of the studied time interval, the nitrogen cycle and ocean redox structure differed from that of a redox-stratified ocean. The Neoproterozoic $\delta^{15}N_{sed}$ distribution with a mode close to +4‰ would be compatible with redox-stratified ocean only if all studied sections (except that of the Rio de la Plata craton with $\delta^{15}N_{ker}$ close to 0‰) were located in the vicinity of upwelling zones, which would be an extraordinary coincidence. Consequently, a globally redox-stratified ocean is an unlikely scenario to explain the Cryogenian-Ediacaran $\delta^{15}N_{sed}$ distribution.

In contrast, the $\delta^{15}N$ distribution for the ~750 to 580 Ma period, while being markedly different from that of OAEs, is strikingly similar to that of modern sediments (Fig. 2a). The most parsimonious hypothesis is thus that it reflects a nitrogen cycle similar to the one operating in the modern ocean, where nitrate was stable throughout the ocean, except in anoxic OMZs and locally restricted anoxic basins. It implies that most of the late Neoproterozoic oceans contained enough dissolved O_2 to stabilize nitrate, with the probable exception of transient OAEs. This interpretation is compatible with the existing knowledge of the redox depositional conditions for the studied samples. Samples from the Araras platform (Amazonian craton) show oxic

409 depositional conditions (Sansjofre et al., 2014), while available data for Svalbard and Canada
410 sections are compatible with deposition under oxygenated conditions or within anoxic OMZs in
411 an otherwise oxygenated ocean. The Datangpo and Doushantuo formations (South China) were
412 both deposited from a redox-stratified water column (Li et al. 2010; Li et a., 2012), yet their
413 $\delta^{15}N_{sed}$ values in both shelf margin and inner-shelf basin settings are positive and lie in the same
414 range as the other locations. These patterns are fully compatible with nitrate having being
415 supplied to these areas through surface currents in a scenario analogous to the present-day anoxic
416 Cariaco Basin, where $\delta^{15}N_{sed}$ values of ~+3.5‰ are maintained (Thunell et al., 2004). The $\delta^{15}N_{sed}$
417 distribution compiled from these locations is thus highly likely to record the $\delta^{15}N$ distribution of
418 the global ocean nitrate inventory, albeit with minor regional influences. As to the negative tail
419 of the distribution defined by samples from the Tamengo Formation deposited in an anoxic basin
420 (Spangenberg et al., 2014), it records the regional signal of N_2-fixation and/or ammonium
421 assimilation expected in the case of redox stratification (Junium and Arthur 2007; Higgins et al.,
422 2012).

423 In detail, the $\delta^{15}N$ distribution for the ~750 to 580 Ma period shows minor differences with the
424 modern distribution. While these differences may simply reflect sampling bias, they may also
425 speak to important differences in the global ocean redox structure, which we explore here.
426 Compared to the modern $\delta^{15}N$ distribution, that of the ~750 to 580 Ma is slightly shifted towards
427 lower $\delta^{15}N_{sed}$ values, its positive tail is less prominent, and its negative tail extends to lower
428 values (as low as -3.3‰; Figs. 2, 7). Its mode is also 1‰ lower than that of modern sediments.
429 This shift to lower $\delta^{15}N_{sed}$ values is compatible with the hypothesis of an oxygenated ocean, but
430 one containing less dissolved oxygen than the modern ocean. Restricted anoxic basins would be
431 more common, increasing the proportion of $\delta^{15}N_{sed}$ values close to 0‰. Similarly, OMZs would

be more widespread and severe, possibly reaching euxinia, which would have resulted in more common quantitative denitrification, hence driving N_2-fixation. O_2 penetration in sediments would also have been less compared to the modern ocean, increasing the surface of sediments experiencing conditions favorable to quantitative sedimentary denitrification. Combined, these effects would have decreased the nitrate inventory of the ocean without significantly increasing residual nitrate $\delta^{15}N$ values, driving N_2-fixation to compensate for the nitrate loss and hence decreasing $\delta^{15}N$ of the global nitrate inventory. Importantly, the absence of marked change in $\delta^{15}N$ signatures during the latter half of the Neoproterozoic (Fig. 4 and Fig. 2f) implies no fundamental and irreversible change in the nitrogen cycle during this interval. These data imply no first order change in oceans redox structure across the NOE and by extension, suggest that pervasive oxygenation of the oceans occurred before 750 Ma.

Few $\delta^{15}N$ data are available for the early Neoproterozoic and late Mesoproterozoic, but significant data have recently been published for the early Mesoproterozoic and Paleoproterozoic (~2.1 to 1.4 Ma; Busigny et al., 2013; Kump et al., 2011; Papineau et al., 2009, 2013; Stüeken, 2013). These data are synthetized in Figure 2g. The mode of the 2.1–1.4 Ga $\delta^{15}N$ distribution is closer to +2‰ compared with +4‰ for the ~750 to 580 Ma period, but is clearly distinct from the -1‰ mode characteristic of the Phanerozoic OAEs. The offset to lower $\delta^{15}N$ values can be interpreted along the same lines of reasoning as above—increased area of restricted anoxic basins and euxinic OMZs, along with less pervasive O_2 penetration in sediments overlain by an oxygenated water column. Redox-stratified restricted basins and OMZs on continental platforms were likely more numerous than during the Neoproterozoic. The extremely large range of $\delta^{15}N$ (from -4 up to +24‰) identified in the Arivilli group (India) may indeed correspond to a restricted anoxic basin or an euxinic OMZ, where the positive $\delta^{15}N$ reflects impingement of the

455 redox transition zone on the surface mixed layer (Papineau et al., 2009, 2013). This interpretation
456 implies a similar N-cycle than in the modern ocean with nitrate being stable in most of the ocean.
457 It is at odds with most previous interpretations of Proterozoic N-cycling which are predicated on
458 the assumption of a redox-stratified ocean. However, recent interpretations of trace metal
459 compilations suggest that a minimum of 60% of the seafloor was overlain by oxygenated waters
460 in the Proterozoic (Partin et al., 2013; Reinhard et al., 2013). This significant revision allows for
461 the possibility that the $\delta^{15}N$ distribution for the 2.1–1.4 Ga period may reflect a modern style N-
462 cycle in pervasively oxygenated oceans.

463 It is difficult to place a quantitative constraint on the dissolved O_2 concentration of Proterozoic
464 oceans given our poor knowledge of the O_2 abundance required to stabilize nitrate.
465 Measurements performed using the recently developed highly sensitive STOX oxygen sensors
466 show that the accumulation of NO_2^-, the intermediate compound associated with N-loss in
467 OMZs, is restricted to O_2 concentrations lower than 50 nM (Thamdrup et al., 2012). A
468 conservative lower estimate for O_2 concentration in a significant part of the oceans between 740
469 and 580 Ma can thus be fixed at 50 nM. However, this is probably underestimated by at least two
470 orders of magnitude, considering that the activity of metabolic pathways controlling N-losses in
471 OMZs have been detected at O_2 concentrations as high as 20 μM (Kalvelage et al., 2011), which
472 prevent NO_2^- accumulation. In any case, the widespread stability of nitrate implies that the
473 Cryogenian and Ediacaran oceans were neither dominantly ferruginous nor sulfidic, because
474 nitrate would have been reduced by ferrous iron or sulfide microbial oxidation, respectively
475 (Canfield et al., 2010; Lavik et al., 2009; Pantke et al., 2012; Weber et al., 2006). Apart from
476 possible episodic OAEs, anoxic waters (ferruginous or sulfidic) must therefore have been
477 restricted to intracratonic and silled basins, zones of widespread upwelling on open continental

shelves, and probably to a thin layer of bottom water overlying the sediment-water interface (Fig. 1d).

5.3. Reconciling Redox Proxies

A host of redox proxy datasets have been published recently for the Neoproterozoic and early Cambrian with seemingly contradictory implications. Compilations of trace metal data from euxinic black shales through time broadly indicate a major oxygenation event sometime in the late Neoproterozoic: the NOE (Fig. 6; Partin et al., 2013; Och and Shields-Zhou, 2012; Scott et al., 2008). Canfield et al. (2007) argued more specifically that deep ocean oxygenation occurred in the middle Ediacaran Period based on a compilation of iron speciation data from the Ediacaran succession of southeast Newfoundland. On the other hand, high-resolution trace metal abundance datasets from the organic-rich Doushantuo Formation in from South China show a prominent spike in Mo, V, and U in the early Ediacaran Period, which imply ocean oxygenation occurred shortly after the Marinoan (end-Cryogenian) glaciation (Sahoo et al., 2012). Other data sets from individual basins variably imply oxic, anoxic, and euxinic continental shelves during the Ediacaran (Johnston et al., 2012, 2013; Li et al., 2010; Sansjofre et al., 2014), while studies of the Precambrian-Cambrian boundary interval indicate ocean anoxia in the late Ediacaran—early Cambrian (Kimura et al., 1997; Schröder and Grotzinger, 2007). Do these seemingly contradictory ocean redox datasets imply that the samples or proxies are unreliable or can these data be reconciled with a single model for Neoproterozoic oxygenation?

We argue for the latter based on the $\delta^{15}N_{sed}$ record. The most parsimonious explanation for the similarity of the $\delta^{15}N_{sed}$ distribution for the 750–580 Ma period to that of modern sediments is that nitrate was largely stable in the Neoproterozoic ocean by ~750 Ma, and hence that the

500 oceans were at least partially oxygenated by this time, albeit likely with low total dissolved
501 oxygen concentrations. If correct this interpretation implies that deep-ocean ventilation occurred
502 prior to the NOE. However, lower ocean O_2 concentrations than in the modern ocean may have
503 allowed for persistent and broad OMZs that produced widespread anoxic conditions on
504 continental shelves, which may even have reached the wind-mixed layer in some occasions as
505 suggested by one reported occurrence of photic zone anoxia biomarkers (Olcott et al., 2005). The
506 extent of anoxia and the occurrence of euxinia, in turn, were dependent on carbon export from
507 the surface ocean, and hence sensitive to local nutrient variability, allowing for variable redox
508 conditions within single basins and between basins. Oxic conditions likely prevailed not only in
509 the surface ocean but also in the deeper ocean and away from highly productive continental
510 margins. However, the sedimentary record of deep Neoproterozoic ocean basins is largely absent
511 from the geological record, accounting for a strong bias in available local redox proxy data
512 towards water column anoxia.

513 Our interpretation is compatible with the latest reinterpretation of trace metal data, recognized
514 proxies for the global ocean redox (Algeo and Rowe, 2011). Reinhard et al. (2013) used a simple
515 mass balance model to show that the low trace metal abundances in black shales prior to 630 Ma
516 allow for a minimum of 60% of the seafloor to have been oxygenated throughout the
517 Proterozoic. Given that the degree to which anoxia and/or euxinia extended into the water
518 column from the seafloor remains completely unconstrained, anoxia may even have been
519 restricted to microbial matts covering the sediment-water interface (Pawlowska et al., 2013) or to
520 a thin layer of bottom water, leaving most of the water column oxygenated enough to allow
521 nitrate accumulation (Fig. 1d). Therefore the unambiguous shift in trace metal abundance at 630
522 Ma (Och and Shields-Zhou, 2012; Partin et al., 2013; Reinhard et al., 2013; Sahoo et al., 2012),

523 rather than heralding deep ocean oxygenation, may instead only record an increase in
524 atmospheric O_2, and hence dissolved O_2, beyond a critical threshold, thereby increasing the
525 penetration depth of O_2 within seafloor sediments and hence total surface area of oxygenated
526 seafloor on continental shelves. This may have been the threshold that permitted the earliest
527 animals to evolve or develop more energy intensive metabolisms, such as burrowing and
528 predation (Sperling et al., 2013).

529 **6. Conclusions**

530 The $\delta^{15}N_{sed}$ datasets presented here (Fig. 2, 4 and 6) suggests that the global nitrogen cycle
531 operated similarly in the second half of the Neoproterozoic Era to in the modern ocean. If true,
532 then it implies that nitrate was stable in the latter Neoproterozoic ocean, which, by extension,
533 was at least mildly oxygenated. This conclusion is compatible with recent modeling of trace
534 element data that suggest that most of the global Proterozoic ocean was sufficiently oxygenated
535 to also accumulate trace metals (Partin et al., 2013; Reinhard et al., 2013). Although this
536 hypothesis does not discount a possible rise in atmospheric and oceanic oxygen levels during this
537 period or significant fluctuations associated with snowball glaciations, it does suggest that the
538 major transition from a dominantly anoxic to oxygenated deep-ocean did not happen between
539 ~750 and 580 Ma but rather sometime prior to 750 Ma, and perhaps much earlier in the
540 Proterozoic.

541 **Acknowledgments**

542 The project was supported by a French MRT doctoral fellowship and a SETSI grant to PS; two
543 INSU (SYSTER) grants as well as an Emergence grant from Paris council (PI Magali Bonifacie)
544 to MA and PS. RIFT and ACRN were supported by the INCT-Geociam program, and by

545 FAPESP and CNPq grants. GPH acknowledges donors of the American Chemical Society
546 Petroleum Research Fund for partial support of this research. GPH benefited from two month of
547 invitation to stay at IPGP. This is IPGP contribution XX.

548 **References**

549 Ader, M., Boudou, J.-P., Javoy, M., Goffe, B., Daniels, E., 1998. Isotope study on organic
550 nitrogen of Westphalian anthracites from the Western Middle field of Pennsylvania (U.S.A.) and
551 from the Bramsche Massif (Germany). Organic Geochemistry 29, 315-323.

552 Ader, M., Cartigny, P., Boudou, J.-P., Oh, J.-H., Petit, E., Javoy, M., 2006. Nitrogen isotopic
553 evolution of carbonaceous matter during metamorphism: Methodology and preliminary results.
554 Chemical Geology 232, 152-169.

555 Ader, M., Macouin, M., Trindade, R.I.F., Hadrien, M.H., Yang, Z., Sun, Z., Besse, J., 2009. A
556 multilayered water column in the Ediacaran Yangtze platform? Insights from carbonate and
557 organic matter paired $\delta^{13}C$. Earth and Planetary Science Letters 288, 213-227.

558 Algeo, T., Rowe, H., Hower, J.C., Schwark, L., Herrmann, A., Heckel, P., 2008. Changes in
559 ocean denitrification during Late Carboniferous glacial–interglacial cycles. Nature geoscience 1,
560 709-714.

561 Algeo, T., Rowe, H., 2012 Paleoceanographic applications of trace-metal concentration data.
562 Chemical Geology 324-325, 6-18.

563 Arnaboldi, M., Meyers, P.A., 2006. Patterns of organic carbon and nitrogen isotopic
564 compositions of latest Pliocene sapropels from six locations across the Mediterranean Sea.
565 Palaeogeography, Palaeoclimatology, Palaeoecology 235, 149–167.

566 Beaumont, V., Robert, F., 1999. Nitrogen isotope ratios of kerogens in Precambrian cherts: a
567 record of the evolution of atmosphere chemistry? Precambrian Research 96, 63-82.

568 Bebout, G.E., Fogel, M.L., 1992. Nitrogen-isotope compositions of metasedimentary rocks in the
569 Catalina Schist, California: Implications for metamorphic devolatilization history. Geochimica et
570 Cosmochimica Acta 56, 2839-2849.

571 Boudou, J.-P., Schimmelmann, A., Ader, M., Mastalerz, M., Sebilo, M., Gengembre, L., 2008.
572 Organic nitrogen chemistry during low-grade metamorphism. Geochimica et Cosmochimica
573 Acta 72, 1199-1221.

574 Boyle, R.A., Clark, J.R., Poulton, S.W., Shields-Zhou, G., Canfield, D.E., Lenton, T.M., 2013.
575 Nitrogen cycle feedbacks as a control on euxinia in the mid-Proterozoic ocean. Nature
576 Communication 4, 1533.

577 Busigny, V., Cartigny, P., Philippot, P., Ader M., Javoy, M., 2003. Massive recycling of nitrogen
578 and other fluid-mobile elements (K, Rb, Cs, H) in a cold slab environment: evidences from HP to

579 UHP oceanic metasediments of the Schistes Lustrés nappe (Western Alps, Europe). Earth and
580 Planetary Science Letters 215, 27-42.

581 Busigny, V., Ader, M., Cartigny, P., 2005. Quantification and isotopic analysis of nitrogen in
582 rocks at the ppm level using sealed tube combustion technique: A prelude to the study of altered
583 oceanic crust. Chemical Geology 223, 249-258.

584 Busigny, V., Lebeau, O., Ader, M., Krapez, B., Bekker, A., 2013. Nitrogen cycle in the Late
585 Archean ferruginous ocean. Chemical Geology 362, 115-130.

586 Butterfield, N.J. 2009. Oxygen, animals and oceanic ventilation: an alternative view. Geobiology
587 7, 1-7.

588 Calvert, S.E., Bustin, R.M., Ingall, E.D., 1996. Influence of water column anoxia and sediment
589 supply on the burial and preservation of organic carbon in marine shales. Geochimica et
590 Cosmochimica Acta 60, 1577-1593.

591 Canfield, D.E., Glazer, A.N., Falkowski, P.G., 2010. The Evolution and Future of Earth's
592 Nitrogen Cycle. Science 330, 192-196.

593 Canfield, D.E., Poulton, S.W., Knoll, A.H., Narbonne, G.M., Ross, G., Goldberg, T., Strauss, H.,
594 2008. Ferruginous Conditions Dominated Later Neoproterozoic Deep-Water Chemistry. Science
595 321, 949-952.

596 Canfield, D.E., Poulton, S.W., Narbonne, G.M., 2007. Late-Neoproterozoic Deep-Ocean
597 Oxygenation and the Rise of Animal Life. Science 315, 92-94.

598 Cao, C., Love, G.D., Hays, L.E., Wang, W., Shen, S., Summons, R.E., 2009. Biogeochemical
599 evidence for euxinic oceans and ecological disturbance presaging the end-Permian mass
600 extinction event. Earth and Planetary Science Letters 281, 188-201.

601 Casciotti, K.L., Sigman, D.M., Ward, B.B., 2003. Linking Diversity and Stable Isotope
602 Fractionation in Ammonia-Oxidizing Bacteria. Geomicrobiology Journal 20, 335-353.

603 Close, H.G., Bovee, R., Pearson, A., 2011. Inverse carbon isotope patterns of lipids and kerogen
604 record heterogeneous primary biomass. Geobiology, 9, 250-265.

605 Cremonese, L., Shields-Zhou, G., Struck, U., Ling, H.-F., Och, L., Chen, X., Li, D., 2013.
606 Marine biogeochemical cycling during the early Cambrian constrained by a nitrogen and organic
607 carbon isotope study of the Xiaotan section, South China. Precambrian Research 225, 148-165.

608 Dumitrescu, M., Brassell, S.C., 2006. Compositional and isotopic characteristics of organic
609 matter for the early Aptian Oceanic Anoxic Event at Shatsky Rise, ODP Leg 198.
610 Palaeogeography, Palaeoclimatology, Palaeoecology 235, 168-191.

611 Farquhar, J., Bao, H., Thiemens, M., 2000. Atmospheric influence of Earth's earliest sulfur
612 cycle. Science 289, 756–758.

613 Fennel, K., Follows, M., Falkowski, P.G., 2005. The co-evolution of the nitrogen, carbon and
614 oxygen cycles in the Proterozoic ocean. American Journal of Science 305, 526-545.

615 Fike, D.A., Grotzinger, J.P., Pratt, L.M., Summons, R.E., 2006. Oxidation of the Ediacaran
616 Ocean. Nature 444, 744-747.

617 Fuchsman, C., Murray, J.W., Konovalov, S.K., 2008. Concentration and natural stable isotope
618 profiles of nitrogen species in the Black Sea. Marine Chemistry 111, 88–103

619 Galbraith, E.D., Sigman, D., Pedersen, T., Robinson, R.S., 2008. Past changes in the marine
620 nitrogen cycle, in: Capone, D., Bronk, D., Mulholland, M., Carpenter, E. (Eds) Nitrogen in the
621 Marine Environment, 2nd edition. Elsevier, pp 1497-1535.

622 Garvin, J., Buick, R., Anbar, A.D., Arnold, G.L., Kaufman, A.J., 2009. Isotopic Evidence for an
623 Aerobic Nitrogen Cycle in the Latest Archean. Science 323, 1045-1048.

624 Godfrey, L.V., Falkowski, P.G., 2009. The cycling and redox state of nitrogen in the Archaean
625 ocean. Nature Geosci 2, 725-729.

626 Godfrey, L.V., Poulton, S.W., Bebout, G.E., Fralick, P.W., 2013. Stability of the nitrogen cycle
627 during development of sulfidic water in the redox-stratified late Paleoproterozoic Ocean.
628 Geology 41, 655-658.

629 Granger, J., Sigman, D.M., Lehmann, M.F., Tortell, P.D., 2008. Nitrogen and oxygen isotope
630 fractionation during dissimilatory nitrate reduction by denitrifying bacteria. Limnol. Oceanogr.,
631 53, 2533–2545.

632 Halverson, G.P., 2011. Glacial sediments and associated strata of the Polarisbreen Group,
633 northeastern Svalbard, in: Arnaud, E., Halverson, G.P., Shields-Zhou, G. (Eds.), The Geological
634 Record of Neoproterozoic Glaciations. Geological Society Memoir 36, London, pp. 571-579.

635 Halverson, G.P. and Shields-Zhou, G., 2011. Chemostratigraphy and the Neoproterozoic
636 glaciations. In: E. Arnaud, G.P. Halverson, and G. Shields-Zhou (Eds.) The Geological Record
637 of Neoproterozoic Glaciations. Geological Society, London, Memoir 36, 51-66.

638 Higgins, M.B., Robinson, R.S., Carter, S.J., Pearson, A., 2010. Evidence from chlorin nitrogen
639 isotopes for alternating nutrient regimes in the Eastern Mediterranean Sea. Earth and Planetary
640 Science Letters 290, 102-107.

641 Higgins, M.B., Robinson, R.S., Husson, J.M., Carter, S.J., Pearson, A., 2012. Dominant
642 eukaryotic export production during ocean anoxic events reflects the importance of recycled
643 NH_4^+. PNAS 109, 2269-2274.

644 Hoffman, P.F., Schrag, D.P., 2002. The snowball Earth hypothesis: testing the limits of global
645 change. Terra Nova 14, 129-155.

646 Jenkyns, H.C., Gröcke, D.R., Hesselbo, S.P., 2001. Nitrogen Isotope Evidence for Water Mass
647 Denitrification during the Early Toarcian (Jurassic) Oceanic Anoxic Event. Paleoceanography
648 16, 593-603.

649 Jenkyns, H.C., Matthews, A., Tsikos, H., Erel, Y., 2007. Nitrate reduction, sulfate reduction, and
650 sedimentary iron isotope evolution during the Cenomanian-Turonian oceanic anoxic event.
651 Paleoceanography 22, PA3208.

652 Jia, Y., 2006. Nitrogen isotope fractionations during progressive metamorphism: A case study
653 from the Paleozoic Cooma metasedimentary complex, southeastern Australia. Geochimica et
654 Cosmochimica Acta 70, 5201-5214.

655 Jia, Y., Kerrich, R., 2004. Nitrogen 15–enriched Precambrian kerogen and hydrothermal
656 systems. Geochemistry, Geophysics, Geosystems 5, Q07005.

657 Johnston, D.T., Poulton, S.W., Goldberg, T., Sergeev, V.N., Podkovyrov, V., Vorob'eva, N.G.,
658 Bekker, A., Knoll, A.H., 2012. Late Ediacaran redox stability and metazoan evolution. Earth and
659 Planetary Science Letters 335-336, 25-35.

660 Johnston, D.T., Poulton, S.W., Tosca, N.J., O'Brien, T., Halverson, G.P., Schrag, D.P.,
661 Macdonald, F.A., 2013. Searching for an oxygenation event in the fossiliferous Ediacaran of
662 northwestern Canada. Chemical Geology. doi: 10.1016/j.chemgeo.2013.08.046.

663 Junium, C.K., Arthur, M.A., 2007. Nitrogen cycling during the Cretaceous, Cenomanian-
664 Turonian Oceanic Anoxic Event II. Geochem. Geophys. Geosyst. 8, Q03002.

665 Kah, L.C., Bartley, J.K., 2011. Protracted oxygenation of the Proterozoic biosphere. International
666 Geology Review 53, 1424-1442.

667 Kalvelage, T., Jensen, M.M., Contreras, S., Revsbech, N.P., Lam, P., Ganter, M., LaRoche, J.,
668 Lavik, G., Kuypers, M.M.M., 2011. Oxygen Sensitivity of Anammox and Coupled N-Cycle
669 Processes in Oxygen Minimum Zones. PLoS ONE 6, e29299.

670 Kikumoto, R., Tahata, M., Nishizawa, M., Sawaki, Y., Maruyama, S., Shu, D., Han, J., Komiya,
671 T., Takai, K., Ueno, Y., 2014. Nitrogen isotope chemostratigraphy of the Ediacaran and Early
672 Cambrian platform sequence at Three Gorges, South China. Gondwana Research, 25, 1057-
673 1069.

674 Kimura, H., Matsumoto, R., Kakuwa, Y., Hamdi, B., and Zibaseresht, H., 1997. The Vendian-
675 Cambrian $\delta^{13}C$ record, North Iran: Evidence for overturning of the ocean before the Cambrian
676 Explosion. Earth and Planetary Science Letters, 147, E1–E7.

677 Kump, L.R., Pavlov, A., and Arthur, M.A., 2005, Massive release of hydrogen sulfide to the
678 surface ocean and atmosphere during intervals of oceanic anoxia: Geology, v. 33, p.397–400.

679 Kump, L., Junium, C., Arthur, M.A., Brasier, A., Fallick, A., Melezhik, V., Lepland, A., Crne,
680 A.E., Luo, G., 2011. Isotopic Evidence for Massive Oxidation of Organic Matter Following the
681 Great Oxidation Event. Science 334, 1694-1696.

682 Kuypers, M.M., van Breugel, Y., Schouten, S., Erba, E., Damsté, J.S.S., 2004. N_2-fixing
683 cyanobacteria supplied nutrient N for Cretaceous oceanic anoxic events. Geology 32, 853-856.

684 Kuypers, M.M., Blokker, P., Hopmans, E.C., Kinkel, H., Pancost, R.D., Schouten, S., Sinninghe
685 Damsté, J.S., 2002. Archaeal remains dominate marine organic matter from the early Albian
686 oceanic anoxic event 1b. Palaeogeography, Palaeoclimatology, Palaeoecology 185, 211-234.

687 Lam P., Lavik, G., Jensen, M.M., van de Vossenberg J., Schmid, M., Woebken, D., Dimitri
688 Gutiérrez D., Amann, R., Jetten, M.S.M., Kuypers, M.M.M., 2009. Revising the nitrogen cycle
689 in the Peruvian oxygen minimum zone. PNAS 106, 4752–4757.

690 Lam, P., Kuypers, M.M.M., 2011. Microbial Nitrogen Cycling Processes in Oxygen Minimum
691 Zones. Marine Science Annual Reviews 3, 317-345.

692 LaPorte, D.F., Holmden, C., Patterson, W.P., Loxton, J.D., Melchin, M.J., Mitchell, C.E.,
693 Finney, S.C., Sheets, H.D., 2009. Local and global perspectives on carbon and nitrogen cycling
694 during the Hirnantian glaciation. Palaeogeography, Palaeoclimatology, Palaeoecology 276, 182-
695 195.

696 Lavik, G., Stuhrmann, T., Bruchert, V., Van der Plas, A., Mohrholz, V., Lam, P., Muszmann, M.,
697 Fuchs, B.M., Amann, R., Lass, U., Kuypers, M.M.M., 2009. Detoxification of sulphidic African
698 shelf waters by blooming chemolithotrophs. Nature 457, 581-584.

699 Lehmann, M.F., Sigman, D.M., McCorkle, D.C., Granger, J., Hoffmann, S., Cane, G., Brunelle,
700 B.G., 2007. The distribution of nitrate $^{15}N/^{14}N$ in marine sediments and the impact of benthic
701 nitrogen loss on the isotopic composition of oceanic nitrate. Geochimica et Cosmochimica Acta
702 71, 5384-5404.

703 Levman, B.G., Bitter, P.H.v., 2002. The Frasnian-Famennian (mid-Late Devonian) boundary in
704 the type section of the Long Rapids Formation, James Bay Lowlands, northern Ontario, Canada.
705 Canadian Journal of Earth Sciences 39, 1795-1818.

706 Li, C., Evans, D.A.D., Halverson, G.P., 2013. Neoproterozoic glaciations in a revised global
707 paleogeography from the breakup of Rodinia to the assembly of Gondwanaland. Sedimentary
708 Geology 294, 219-232.

709 Li, C., Love, G.D., Lyons, T.W., Fike, D.A., Sessions, A.L., Chu, X., 2010. A Stratified Redox
710 Model for the Ediacaran Ocean. Science 328, 80-83.

711 Li, C., Love, G.D., Lyons, T.W., Scott, C.T., Feng, L., Huang, J., Chang, H., Zhang, Q., Chu, X.,
712 2012. Evidence for a redox stratified Cryogenian marine basin, Datangpo Formation, South
713 China. Earth and Planetary Science Letters 331-332, 246-256.

714 Logan, G.A., Hayes, J.M., Hieshima, G.B., Summons, R.E., 1995. Terminal Proterozoic
715 reorganization of biogeochemical cycles. Nature 376, 53-56.

716 Luo, G., Wang, Y., Algeo, T.J., Kump, L.R., Bai, X., Yang, H., Yao, L., Xie, S., 2011. Enhanced
717 nitrogen fixation in the immediate aftermath of the latest Permian marine mass extinction.
718 Geology 39, 647-650.

719 Lyons, T.W., Reinhard, C.T., Planavsky., N.J., 2014. The rise of oxygen in Earth's early ocean
720 and atmosphere. Nature 506, 307–315.

721 Macdonald, F. A., Schmitz, M. D., Crowley, J. L., Roots, C. F., Jones, D. S., Maloof, A. C.,
722 Strauss, J. V., Cohen, P. A., Johnston, D. T., and Schrag, D. P., 2010. Calibrating the
723 Cryogenian: Science 327, 1241-1243.

724 Macouin, M., Besse, J., Ader, M., Gilder, S., Yang, Z., Sun, Z., Agrinier, P., 2004. Combined
725 paleomagnetic and isotopic data from the Doushantuo carbonates, South China: implications for
726 the "snowball Earth" hypothesis. Earth Planet. Sci. Lett. 224, 387-398.

727 Mandernack, K.W., Mills, C.T., Johnson, C.A., Rahn, T., Kinney, C., 2009. The $\delta^{15}N$ and $\delta^{18}O$
728 values of N_2O produced during the co-oxidation of ammonia by methanotrophic bacteria.
729 Chemical Geology 267, 96–107.

730 Mariotti, A., Germon, J.C., Hubert, P., Kaiser, P., Letolle, R., Tardieux, A., Tardieux, P., 1981.
731 Experimental determination of nitrogen kinetic isotope fractionation: Some principles;
732 illustration for the denitrification and nitrification processes. Plant and Soil 62, 413-430.

733 McFadden, K.A., Huang, J., Chu, X., Jiang, G., Kaufman, A.J., Zhou, C., Yuan, X., Xiao, S.,
734 2007. Pulsed oxidation and biological evolution in the Ediacaran Doushantuo Formation. PNAS
735 105, 3197-3202.

736 Meckler, A.N., Haug, G.H., Sigman, D.M., Plessen, B., Petersen, L.C., Thierstein, H.R., 2007.
737 Detailed sedimentary N isotope records from Cariaco Basin for Terminations I and V: Local and
738 global implications. Global Biogeochem. Cycles 21, GB4019.

739 Meyers, P.A., 2006. Paleoceanographic and paleoclimatic similarities between Mediterranean
740 sapropels and Cretaceous black shales. Palaeogeography, Palaeoclimatology, Palaeoecology 235,
741 305-320.

742 Meyers, P.A., Bernasconi, S.M., 2005. Carbon and nitrogen isotope excursions in mid-
743 Pleistocene sapropels from the Tyrrhenian Basin: Evidence for climate-induced increases in
744 microbial primary production. Marine Geology 220, 41-58.

745 Mingram, B., Brauer, K., 2001. Ammonium concentration and nitrogen isotope composition in
746 metasedimentary rocks from different tectonometamorphic units of the European Variscan Belt.
747 Geochimica et Cosmochimica Acta 65, 273-287.

748 Möbius, J., 2013. Isotope fractionation during nitrogen remineralization (ammonification):
749 Implications for nitrogen isotope biogeochemistry. Geochimica et Cosmochimica Acta 105, 422–
750 432.

751 Narbonne, G.M., Gehling, J.G., 2003. Life after snowball: The oldest complex Ediacaran fossils.
752 Geology 31, 27-30.

753 Och, L.M., Shields-Zhou, G.A., 2012. The Neoproterozoic oxygenation event: Environmental
754 perturbations and biogeochemical cycling. Earth-Science Reviews 110, 26-57.

755 Olcott, A.N., Sessions, A.L., Corsetti, F.A., Kaufman, A.J., de Oliviera, T.F., 2005. Biomarker
756 Evidence for Photosynthesis During Neoproterozoic Glaciation. Science 310, 471-474.

757 Pantke, C., Obst, M., Benzerara, K., Morin, G., Ona-Nguema, G., Dippo, U., Kappler, A., 2012.
758 Green Rust during Fe(II) Oxidation by Nitrate-ReducingAcidovoraxsp. Strain BoFeN1.
759 Environmental Science and Technology 46, 1439-1446.

760 Papineau, D., Purohit, R., Goldberg, T., Pi, D., Shields, G.A., Bhu, H., Steele, A., Fogel, M.L.,
761 2009. High primary productivity and nitrogen cycling after the Paleoproterozoic phosphogenic
762 event in the Aravalli Supergroup, India. Precambrian Research 171, 37-56.

763 Papineau, D., Purohit, R., Fogel, M.L., Shields-Zhou, G.A., 2013. High phosphate availability as
764 a possible cause for massive cyanobacterial production of oxygen in the Paleoproterozoic
765 atmosphere. Earth and Planetary Science Letters 362, 225–236.

766 Partin, C.A., Bekker, A., Planavsky, N.J., Scott, C.T., Gill, B.C., Li, C., Podkovyrov, V., Maslov,
767 A., Konhauser, K.O., Lalonde, S.V., Love, G.D., Poulton, S.W., Lyons, T.W., 2013. Large-scale
768 fluctuations in Precambrian atmospheric and oceanic oxygen levels from the record of U in
769 shales. Earth and Planetary Science Letters 369-370, 284-293.

770 Pawlowska, M.M., Butterfield, N.J., Brocks, J.J., 2013. Lipid taphonomy in the Proterozoic and
771 the effect of microbial mats on biomarker preservation. Geology 41, 103–106.

772 Pennock, J.R., Velinsky, D.J., Ludlam, J.M., Sharp, J.H., Fogel, M.L., 1996. Isotopic
773 fractionation of ammonium and nitrate during uptake by *Skeletonema costatum*: Implications for
774 $\delta^{15}N$ dynamics under bloom conditions. Limnology and Oceanography 41, 451-459.

775 Pinti, D.L., Hashizume, K. Sugihara, A., Massault, M., Philippot, P., 2009. Isotopic fractionation
776 of nitrogen and carbon in Paleoarchean cherts from Pilbara craton, Western Australia: Origin of
777 ^{15}N-depleted nitrogen. Geochimica et Cosmochimica Acta 73, 3819–3848.

778 Planavsky, N.J., McGoldrick, P., Scott, C.T., Li, C., T. Reinhard, C.T., Kelly, A.E., Chu, X.,
779 Bekker, A., Love, G.D., W. Lyons, T.W., 2011. Widespread iron-rich conditions in the mid-
780 Proterozoic ocean. Nature 477, 448-451.

781 Poulton, S.W., Canfield, D.E., 2011. Ferruginous conditions: a dominant feature of the Ocean
782 through Earth's history. Elements 7, 107-112.

783 Quan, T.M., Falkowski, P.G., 2009. Redox control of N:P ratios in aquatic ecosystems.
784 Geobiology 7, 124-139.

785 Quan, T.M., van de Schootbrugge, B., Field, M.P., Rosenthal, Y., Falkowski, P.G., 2008.
786 Nitrogen isotope and trace metal analyses from the Mingolsheim core (Germany): Evidence for
787 redox variations across the Triassic-Jurassic boundary. Global Biogeochem. Cycles 22, GB2014.

788 Reinhard, C.T., Planavsky, N.J., Robbins, L.J., Partin, C.A., Gill, B.C., Lalonde, S.V., Bekker,
789 A., Konhauser, K.O., Lyons, T.W., 2013. Proterozoic ocean redox and biogeochemical stasis.
790 Proceedings of the National Academy of Sciences 110, 5357-5362.

791 Robinson, R.S., Kienast, M., Luiza Albuquerque, A., Altabet, M., Contreras, S., De Pol Holz, R.,
792 Dubois, N., Francois, R., Galbraith, E., Hsu, T.-C., Ivanochko, T., Jaccard, S., Kao, S.-J., Kiefer,
793 T., Kienast, S., Lehmann, M., Martinez, P., McCarthy, M., Möbius, J., Pedersen, T., Quan, T.M.,
794 Ryabenko, E., Schmittner, A., Schneider, R., Schneider-Mor, A., Shigemitsu, M., Sinclair, D.,
795 Somes, C., Studer, A., Thunell, R., Yang, J.-Y., 2012. A review of nitrogen isotopic alteration in
796 marine sediments. Paleoceanography 27, PA4203.

797 Sachs, J.P., Repeta, D.J., Goericke, R., 1999. Nitrogen and carbon isotopic ratios of chlorophyll
798 from marine phytoplankton. Geochimica et Cosmochimica Acta 63, 1431-1441.

799 Sahoo, S.K., Planavsky, N.J., Kendall, B., Wang, X., Shi, X., Scott, C., Anbar, A.D., Lyons,
800 T.W., Jiang, G., 2012. Ocean oxygenation in the wake of the Marinoan glaciation. Nature 489,
801 546-549.

802 Sansofre, P., 2011. L'environnement post-marinoen (ca. 635 ma) : une étude multi-proxy de la
803 plateforme carbonatée du Groupe d'Araras (Mato Grosso, Brésil). PhD thesis, Université Paris-
804 Diderot, pp 287.

805 Sansjofre, P., Ader, M., Trindade, R.I.F., Elie, M., Lyons, J., Cartigny, P., Nogueira, A.C.R.,
806 2011. A carbon isotope challenge to the snowball Earth. Nature 478, 93-96.

807 Sansjofre, P., Trindade, R.I.F., Ader, M., Soares, J.L., Nogueira, A.C.R., Tribovillard, N., 2014.
808 Paleoenvironmental reconstruction of the Ediacaran Araras platform (Western Brazil) from the
809 sedimentary and trace metals record. Precambrian Research, 241, 185-202.

810 Santoro, A.E., Casciotti, K.L., 2011. Enrichment and characterization of ammonia-oxidizing
811 archaea from the open ocean: phylogeny, physiology and stable isotope fractionation. ISME J 5,
812 1796-1808.

813 Scholz, F., Severmann, S., McManus, J., Hensen, C., 2014. Beyond the Black Sea paradigm: The
814 sedimentary fingerprint of an open-marine iron shuttle. Geochimica et Cosmochimica Acta 127,
815 368-380.

816 Schroder, S., Grotzinger, J.P., 2007. Evidence for anoxia at the Ediacaran-Cambrian boundary:
817 the record of redox-sensitive trace elements and rare earth elements in Oman. Journal of
818 Geological Society of London 164, 175-187.

819 Scott, C., Lyons, T.W., Bekker, A., Shen, Y., Poulton, S.W., Chu, X., Anbar, A.D., 2008.
820 Tracing the stepwise oxygenation of the proterozoic ocean. Nature 452, 456-459.

821 Shen, B., Xiao, S., Bao, H., Kaufman, A.J., Zhou, C., Yuan, X., 2011. Carbon, sulfur, and
822 oxygen isotope evidence for a strong depth gradient and oceanic oxidation after the Ediacaran
823 Hankalchough glaciation? Geochimica et Cosmochimica Acta 75, 1357–1373.

824 Sigman, D.M., DiFiore, P.J., Hain, M.P., Deutsch, C., Wang, Y., Karl, D.M., Knapp, A.N.,
825 Lehmann, M.F., Pantoja, S., 2009a. The dual isotopes of deep nitrate as a constraint on the cycle
826 and budget of oceanic fixed nitrogen. Deep Sea Research Part I: Oceanographic Research Papers
827 56, 1419-1439.

828 Sigman, D.M., Karsh, K.L., Casciotti, K.L., 2009b. Nitrogen isotopes in the ocean, in: Steele,
829 J.H., Thorpe, S.A., Turekian, K.K. (Eds) Encyclopedia of Ocean Sciences. Academic Press,
830 Oxford, pp. 40–54.

831 Sliwinski, M.G., Whalen, M.T., Newberry, R.J., Payne, J.H., Day, J.E., 2011. Stable isotope
832 (δ^{13}Ccarb and org, δ^{15}Norg) and trace element anomalies during the Late Devonian 'punctata
833 Event' in the Western Canada Sedimentary Basin. Palaeogeography, Palaeoclimatology,
834 Palaeoecology 307, 245-271.

Somes, C.J., Schmittner, A., Galbraith, E.D., Lehmann, M.F., Altabet, M.A., Montoya, J.P., Letelier, R.M., Mix, A.C., Bourbonnais, A., Eby, M., 2010. Simulating the global distribution of nitrogen isotopes in the ocean. Global Biogeochem. Cycles 24, GB4019.

Spangenberg, J.E., Bagnoud-VelÃ¡squez, M., Boggiani, P.C., Gaucher, C., 2014. Redox variations and bioproductivity in the Ediacaran: Evidence from inorganic and organic geochemistry of the Corumbá Group, Brazil. Gondwana Research. doi 10.1016/j.gr.2013.08.014.

Sperling, E.A., Halverson, G.P., Knoll, A.H., Macdonald, F.A., Johnston, D.T., 2013. A basin redox transect at the dawn of animal life. Earth and Planetary Science Letters 371-372, 143-155.

Stüeken, E.E., 2013. A test of the nitrogen-limitation hypothesis for retarded eukaryote radiation: Nitrogen isotopes across a Mesoproterozoic basinal profile. Geochimica et Cosmochimica Acta 120, 121-139.

Tesdal, J.E., Galbraith, E.D., Kienast, M., 2013. Nitrogen isotopes in bulk marine sediment: linking seafloor observations with subseafloor records. Biogeosciences 10, 101-118.

Thamdrup, B., Dalsgaard, T., Revsbech, N.P., 2012. Widespread functional anoxia in the oxygen minimum zone of the Eastern South Pacific. Deep Sea Research Part I: Oceanographic Research Papers 65, 36-45.

Thomazo, C., Ader, M., Philippot, P., 2011. Extreme ^{15}N-enrichments in 2.72-Gyr-old sediments: evidence for a turning point in the nitrogen cycle. Geobiology 9, 107-120.

Thomazo, C., Pinti, D.L., Busigny, V., Ader, M., Hashizume, K., Philippot, P., 2009. Biological activity and the Earth's surface evolution: Insights from carbon, sulfur, nitrogen and iron stable isotopes in the rock record. Comptes Rendus Palevol 8, 665-678.

Thunell, R.C., Sigman, D.M., Muller-Karger, F., Astor, Y., Varela, R., 2004. Nitrogen isotope dynamics of the Cariaco Basin, Venezuela. Global Biogeochem. Cycles 18, GB3001.

Voss, M., Dippner, J.W., Montoya, J.P., 2001. Nitrogen isotope patterns in the oxygen-deficient waters of the Eastern Tropical North Pacific Ocean. Deep Sea Research Part I: Oceanographic Research Papers 48, 1905-1921.

Wang, L., Shi, X., Jiang, G., 2012. Pyrite morphology and redox fluctuations recorded in the Ediacaran Doushantuo Formation. Palaeogeography, Palaeoclimatology, Palaeoecology 333, 218–227.

Weber, K.A., Achenbach, L.A., Coates, J.D., 2006. Microorganisms pumping iron: anaerobic microbial iron oxidation and reduction. Nat Rev Micro 4, 752-764.

Wenk, C.B., Blees, J., Zopfi, J., Veronesi, M.L., Bourbonnais, A., Schubert, C.J., Niemann, H., Lehmann, M.F., 2013. Anaerobic ammonium oxidation (anammox) bacteria and sulfide-dependent denitrifiers coexist in the water column of a meromictic south-alpine lake. Limnology and Oceanography, 58, 1–12.

Wenk, C.B., Zopfi, J., Blees, J., Veronesi, M., Niemann, H., Lehmann, M.F., 2014. Community N and O isotope fractionation by sulfide-dependent denitrification and anammox in a stratified lacustrine water column. Geochimica et Cosmochimica Acta, 125, 551–563

Yui, T.-F., Kao, S.-J., Wu, T.-W., 2009. Nitrogen and N-isotope variation during low-grade metamorphism of the Taiwan mountain belt. Geochemical Journal 43, 15-27.

Zerkle, A.L., Junium, C.K., Canfield, D.E., House, C.H., 2008. Production of ^{15}N-depleted biomass during cyanobacterial N_2-fixation at high Fe concentrations. J. Geophys. Res. 113, G03014.

Figure legends

Figure 1: Schematic representation of the nitrogen cycle and resulting nitrogen-isotopic imprint on marine sediments (a) in a modern-like oxic ocean in which oxygen penetrates into the sediment except in OMZs where denitrification does not reach completion, (b) in a redox-stratified ocean with a relatively deep redox transition zone, where nitrate and ammonium are quantitatively converted to N_2/N_2O at the redox transition zone, except at vigorous upwelling locations where ammonium is nitrified concurrently with conversion to gaseous species, (c) in a redox stratified ocean with a shallow redox transition zone stabilizing below the surface mixed layer, except in upwelling zones where anoxic waters may reach the surface, allowing ammonium to be assimilated at the same time as being converted to N_2 and N_2O, c) in our model for the 750 to 580 Ma ocean with extended and severely OMZz and limited oxygen penetration in surface sediments. The red color indicates anoxic waters and the blue color oxygenated waters. $\varepsilon_{ap} \approx 0$ indicates cases where the reaction is complete so that the apparent isotope fractionation (ε_{ap}) is close to nil.

894 **Figure 2**: Comparison of $\delta^{15}N_{sed}$ distribution in modern oceanic sediments, in Phanerozoic
895 anoxic events and in Neoproterozoic sediments. (a) Modern sediment $\delta^{15}N_{sed}$, modified after
896 Tesdal et al. (2013). (b) $\delta^{15}N_{sed}$ from anoxic events in the Phanerozoic: (i) in black, the
897 Cretaceous ocean anoxic events OAEs 1a, 1b, 1d and 2 (Arnaboldi and Meyers, 2006;
898 Dumitrescu and Brassel, 2006; Jenkyns et al., 2007; Junium and Arthur, 2007; Kuypers et al.,
899 2002, 2004; Meyers 2006); (ii) in dark grey, early Toarcian OAE (T-OAE) (Jenkyns et al.,
900 2001); (iii) in light grey, the Quaternary and Cenozoic Mediterranean sapropels (Higgins et al.,
901 2010; Meyers and Bernasconi, 2005; Sachs et al., 1999); (iv) in white, other Phanerozoic anoxic
902 events, of unknown spatial extent, which correspond to the Triassic-Jurassic transition (Quan et
903 al., 2008), the Permian-Triassic transition (Cao et al., 2009; Luo et al., 2011), the late Devonian
904 (Calvert et al., 1996; Levman and Bitter, 2002; Sliwinski et al., 2011), the late Ordovician
905 (LaPorte et al., 2009) and the early Cambrian (Cremonese et al., 2013). (c) Histogram of the
906 $\delta^{15}N_{sed}$ data for the Yangtze platform (South China craton): in grey, data from the Yangjiaping
907 section representative of the shelf margin (this study), in white, previously published data from
908 the top of the Dengying Formation in the Xiaotan section (Cremonese et al., 2013) and the
909 Doushantuo and Dengying formations in the Wuhe section, representative of the inner shelf
910 basin (Kikumoto et al., 2014). (d) $\delta^{15}N_{sed}$ distributions for Brazil: in black, data from the Amazon
911 craton (this study); in white, $\delta^{15}N_{kerogen}$ values reported for the Tamengo Formation, Rio de la
912 Plata craton (Spangenberg et al., 2014). (e) $\delta^{15}N_{sed}$ values for northwestern Canada (white) and
913 Svalbard (grey). (f) Histogram of all the $\delta^{15}N_{sed}$ (and $\delta^{15}N_{kerogen}$) data obtained in this study
914 compiled with the previous late Neoproterozoic data (Cremonese et al., 2013; Kikumoto et al.,
915 2014; Spangenberg et al., 2014). (g) Histogram of published $\delta^{15}N_{sed}$ and $\delta^{15}N_{kerogen}$ data for
916 Paleoproterozoic and Mesoproterozoic successions: 1.4–1.5 Ga Belt Basin, Montana ($\delta^{15}N_{sed}$

from Stüeken et al., 2013); 1.8–1.9 Ga Animikie Basin, North America ($\delta^{15}N_{sed}$ from Godfrey et al., 2013); 2.0–2.1 Ga Onega Basin, NW Russia ($\delta^{15}N_{kerogen}$ from Kump et al., 2011) and 1.9–2.1 Ga Aravilli group, India ($\delta^{15}N_{sed}$ from Papineau et al., 2009, 2013).

Figure 3: Paleogeographic reconstruction for 630 Ma (Modified from Li et al., 2013). Red empty stars indicate the locations of the four sample sets (South China, Amazon, NW Canada and NE Svalbard).

Figure 4: Chemostratigraphic representation of the present study $\delta^{15}N_{sed}$ results together with available $\delta^{13}C_{carb}$ and $\delta^{13}C_{org}$ data. (a–c) Sections spanning the Araras platform on the southeastern margin of the Amazonian craton (Fig. S1): (a) Composite Terconi-Camil section; (b) Carmelo section; (c) Copacel section. For Camil, Carmelo and Copacel sections, $\delta^{13}C_{carb}$ and $\delta^{13}C_{org}$ are from Sansjofre (2011) and for Terconi section from Sansjofre et al. (2011). (d) Yangjiaping section, Shelf margin of the Yangtze platform, South China craton. $\delta^{13}C_{carb}$ and $\delta^{13}C_{org}$ are from Macouin et al. (2004) and Ader et al. (2009). (e) Composite northeast Svalbard section. Previously published $\delta^{13}C_{carb}$ and $\delta^{13}C_{org}$ are from Halverson (2011). (f) Composite northwest Canada section. $\delta^{13}C_{carb}$ are from Hoffman and Schrag (2002).

Figure 5: N and $\delta^{15}N_{sed}$ data analyses. (a) Cross-plots of $\delta^{15}N_{sed}$ values with the nitrogen content in ppm in the decarbonated residue (N_{decarb} ppm). (b) Cross-plots of $\delta^{15}N_{sed}$ values with C/N. (c) Cross-plots of N_{decarb} ppm with TOC_{decarb} ppm in log scales showing a broad correlation passing

938 through the origin, as expected in the case of an organic origin for the sedimentary nitrogen. (d)
939 Cross-plots of $\delta^{15}N_{sed}$ values with $\delta^{13}C_{org}$ showing no correlation.

940

941 **Figure 6**: Summary figure showing the major features of biospheric and paleoenvironmental
942 evolution from the early Neoproterozoic to the early Cambrian. Ranges of eukaryotes
943 summarized from Macdonald et al. (2010). Composite carbonate $\delta^{13}C$ profile modified from
944 Halverson and Shields-Zhou (2011). Mo concentrations in euxinic black shales from Sahoo et al.
945 (2012). Nitrogen isotope data from this contribution, Cremonese et al. (2013), Kikumoto et al.
946 (2014), and Spangenberg et al. (2014).

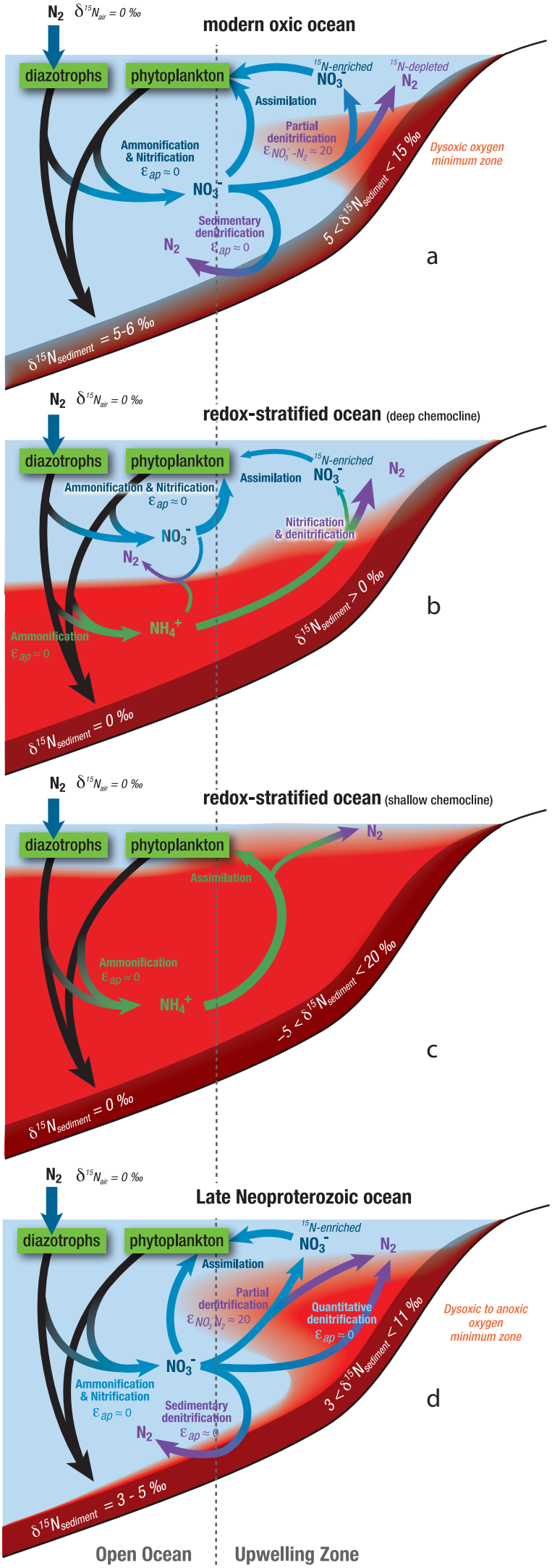
modern oxic ocean
diazotrophs
phytoplankton
Assimilation
Ammonification & Nitrification
Partial denitrification
Sedimentary denitrification
Dysoxic oxygen minimum zone
a
redox-stratified ocean (deep chemocline)
Nitrification & denitrification
Ammonification
b
redox-stratified ocean (shallow chemocline)
c
Late Neoproterozoic ocean
Quantitative denitrification
Dysoxic to anoxic oxygen minimum zone
d
Open Ocean
Upwelling Zone

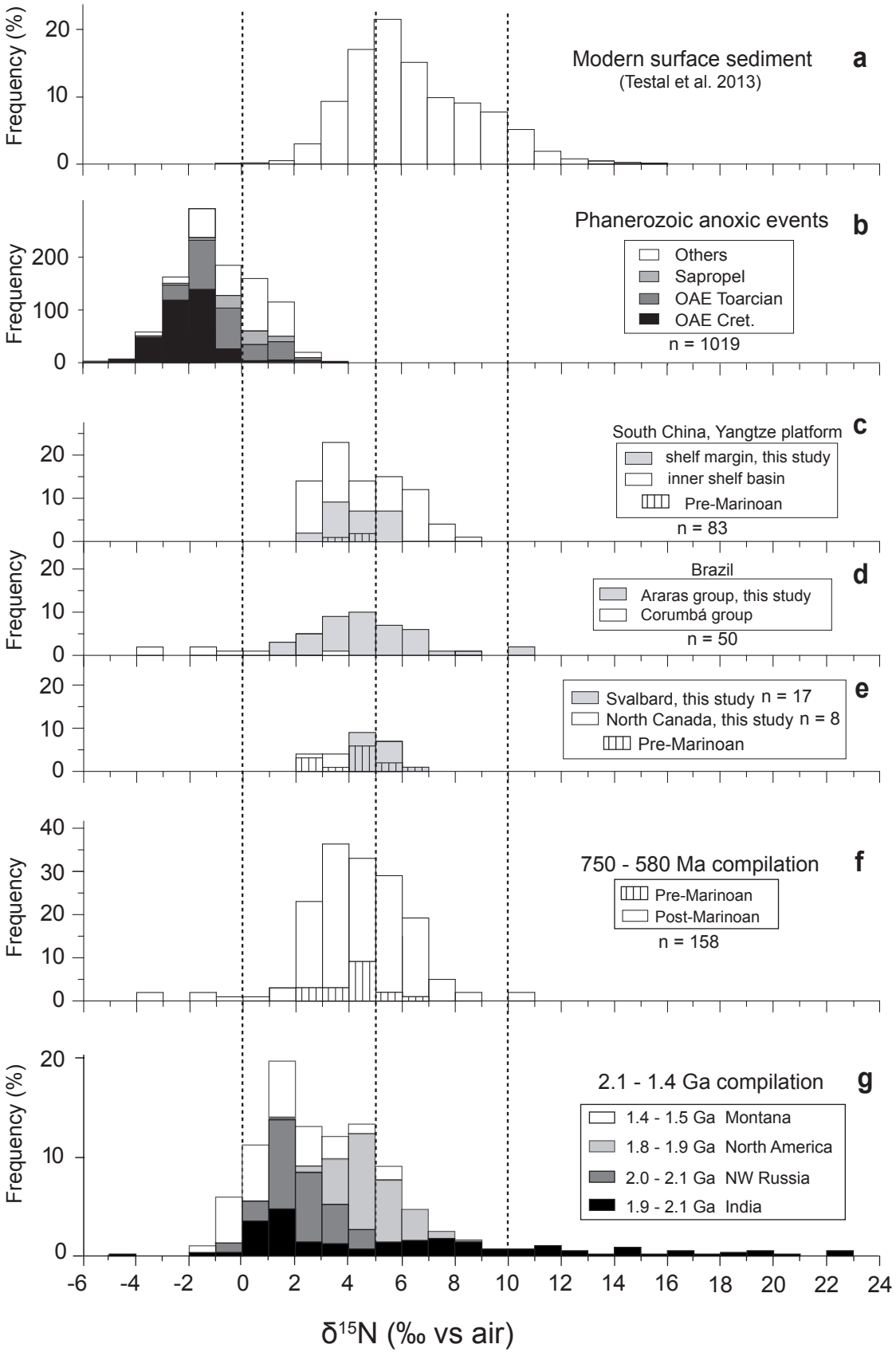
Frequency (%)
Modern surface sediment
(Testal et al. 2013)
a
Phanerozoic anoxic events
b
Others
Sapropel
OAE Toarcian
OAE Cret.
n = 1019
Frequency
South China, Yangtze platform
c
shelf margin, this study
inner shelf basin
Pre-Marinoan
n = 83
Brazil
d
Araras group, this study
Corumbá group
n = 50
e
Svalbard, this study n = 17
North Canada, this study n = 8
Pre-Marinoan
750 - 580 Ma compilation
f
Pre-Marinoan
Post-Marinoan
n = 158
2.1 - 1.4 Ga compilation
g
1.4 - 1.5 Ga Montana
1.8 - 1.9 Ga North America
2.0 - 2.1 Ga NW Russia
1.9 - 2.1 Ga India
δ15N (‰ vs air)

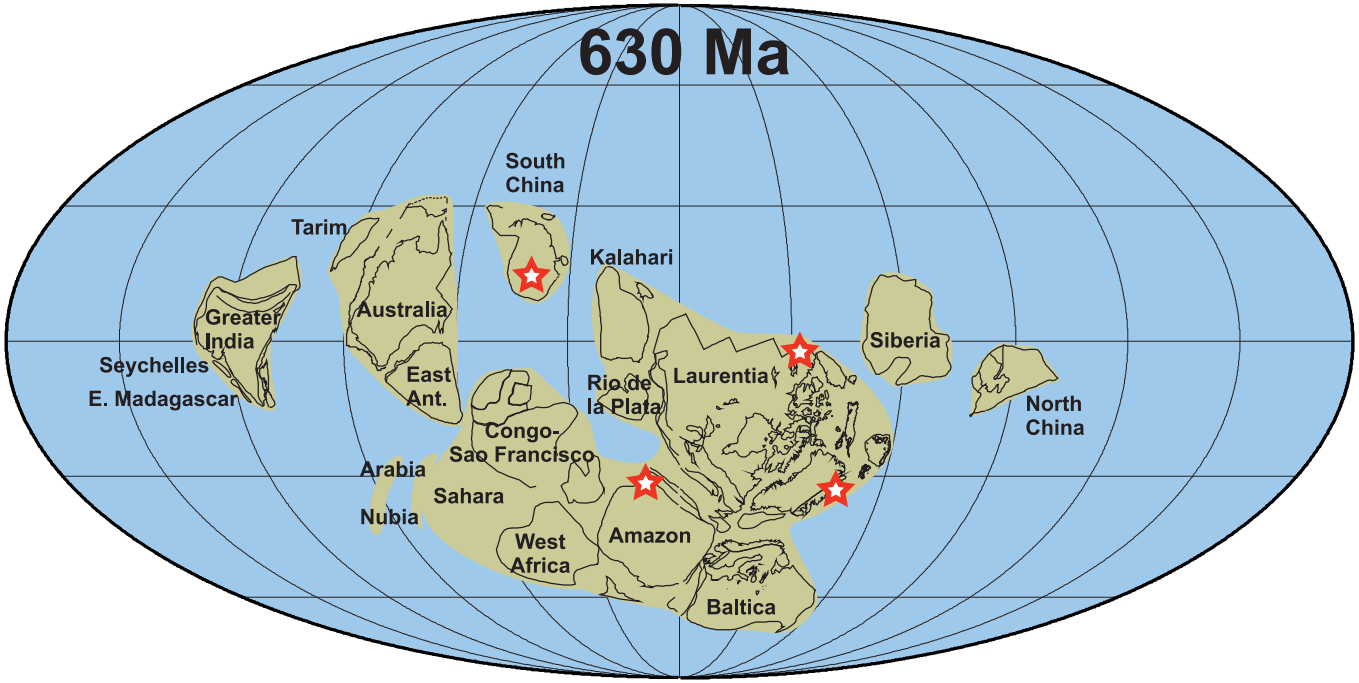
630 Ma
South China
Tarim
Kalahari
Australia
Greater India
Seychelles
E. Madagascar
East Ant.
Rio de la Plata
Laurentia
Siberia
North China
Congo-Sao Francisco
Arabia
Sahara
Nubia
West Africa
Amazon
Baltica

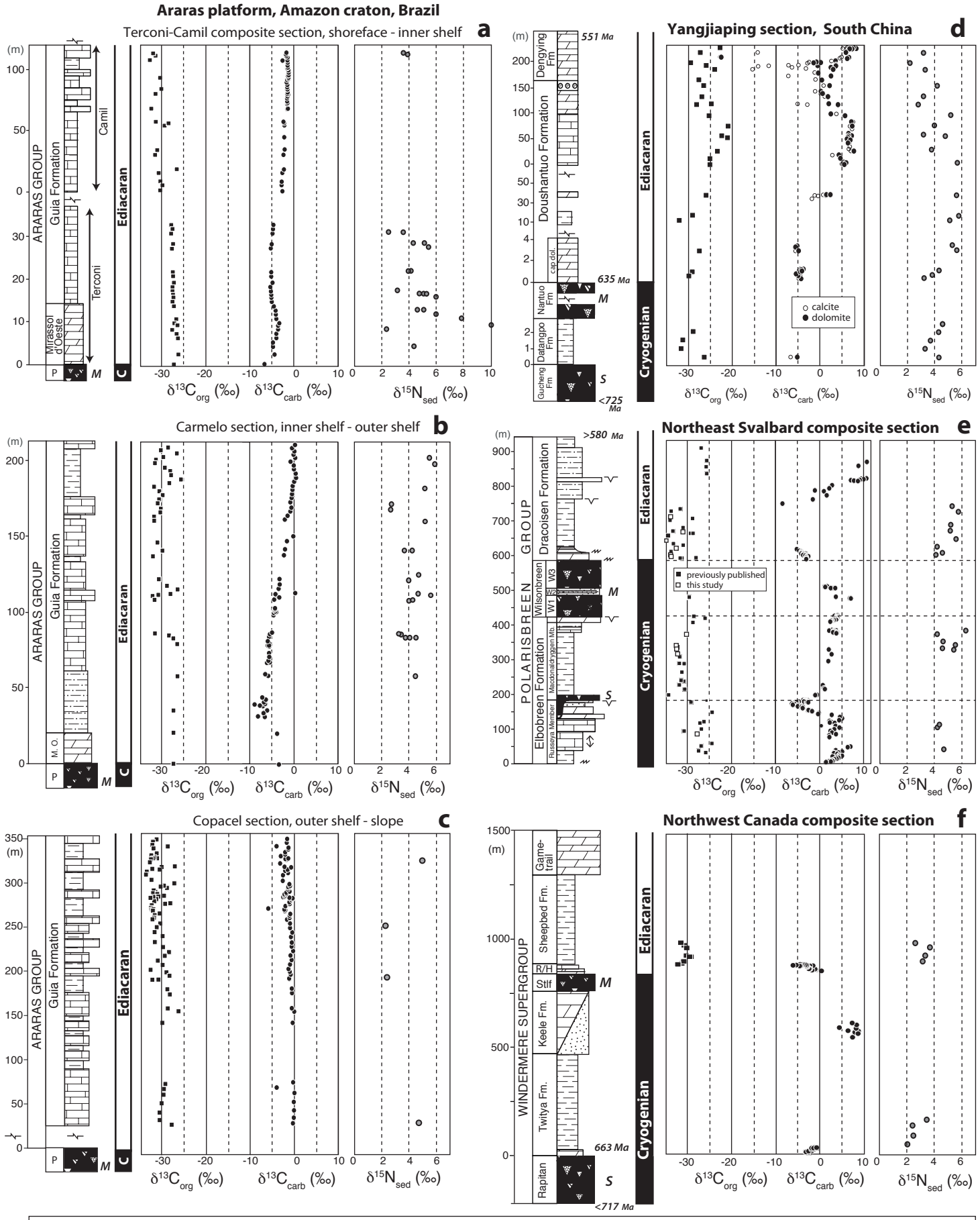
Araras platform, Amazon craton, Brazil
Terconi-Camil composite section, shoreface - inner shelf
a
ARARAS GROUP
Guia Formation
Camil
Terconi
Mirassol d'Oeste
P
M
C
Ediacaran
δ13Corg (‰)
δ13Ccarb (‰)
δ15Nsed (‰)
551 Ma
Dengying Fm
Doushantuo Formation
cap dol.
635 Ma
Nantuo Fm
Datangpo Fm
Gucheng Fm
<725 Ma
Ediacaran
Cryogenian
Yangjiaping section, South China
d
calcite
dolomite
Carmelo section, inner shelf - outer shelf
b
M. O.
>580 Ma
GROUP
Dracoisen Formation
POLARISBREEN
Wilsonbreen
W3
W2
W1
Elobreen Formation
Macdonaldryggen Mb.
Russøya Member
Northeast Svalbard composite section
e
previously published
this study
Copacel section, outer shelf - slope
c
WINDERMERE SUPERGROUP
Gametrail
Sheepbed Fm.
R/H
Stlf
Keele Fm.
Twitya Fm.
Rapitan
663 Ma
<717 Ma
Northwest Canada composite section
f
glacigenic
sandstone
siltstone
shale
dolomite
limestone
phosphorite
not exposed
exposure surface
flooding surface
molar tooth structures

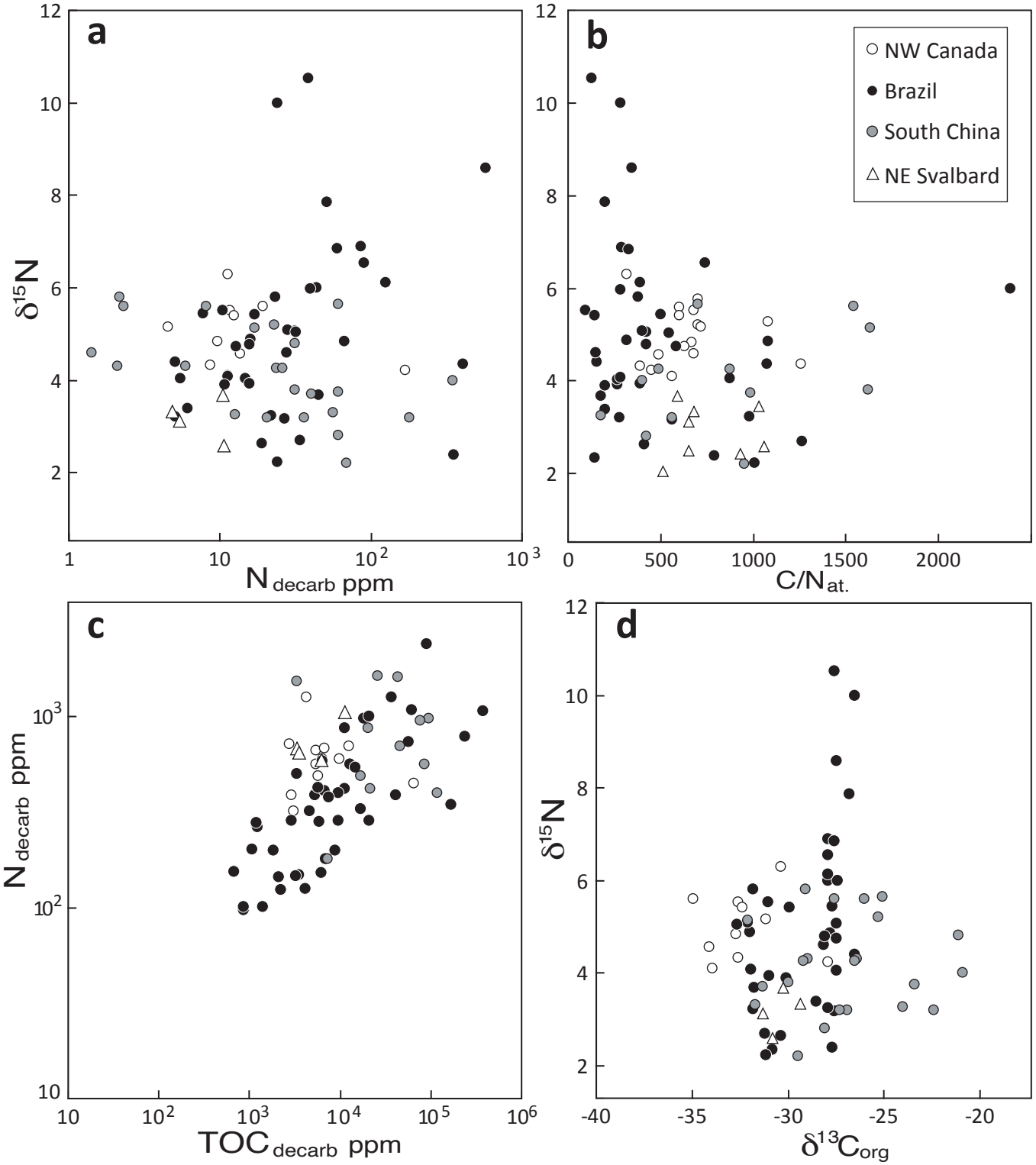
a
b
c
d
NW Canada
Brazil
South China
NE Svalbard
δ15N
N decarb ppm
C/Nat.
TOC decarb ppm
δ13Corg

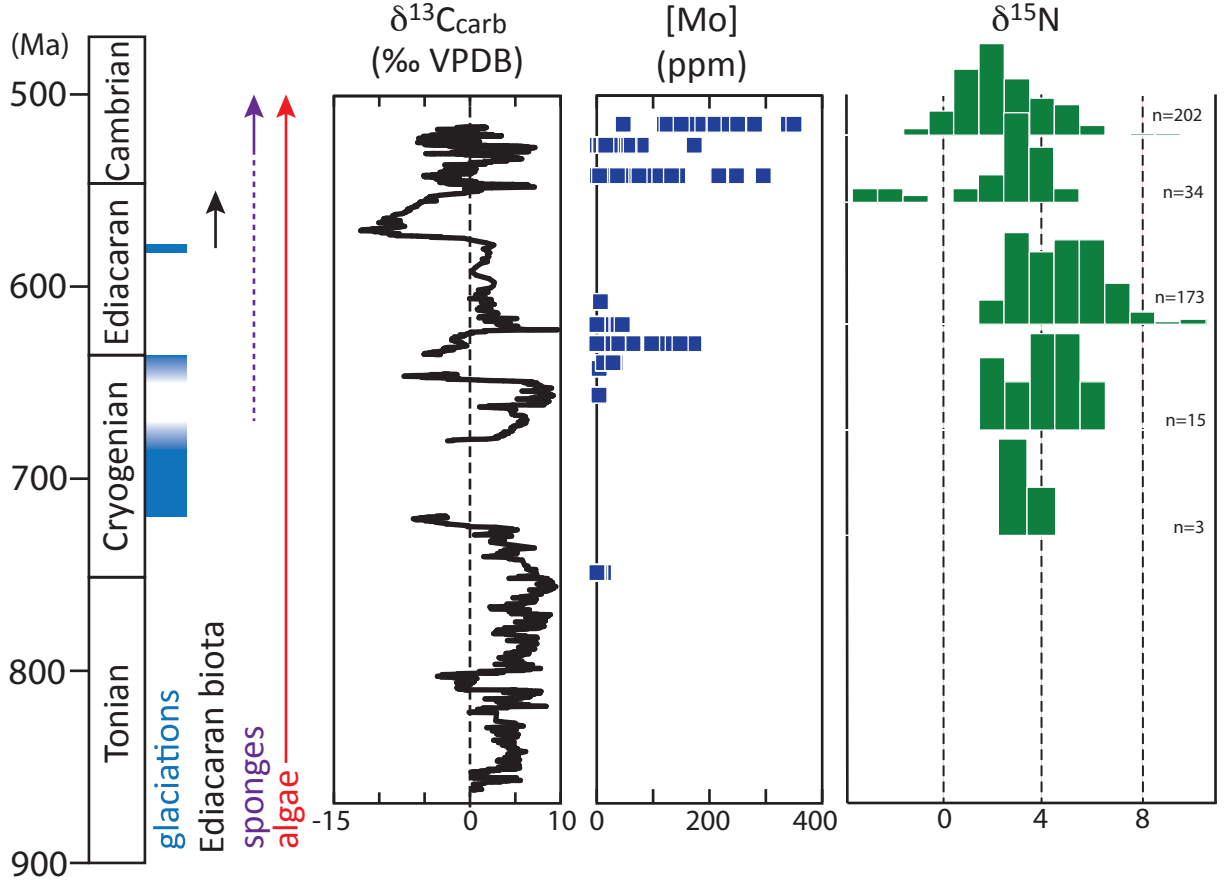
(Ma)
500
600
700
800
900
Cambrian
Ediacaran
Cryogenian
Tonian
glaciations
Ediacaran biota
sponges
algae
δ13Ccarb
(‰ VPDB)
-15
0
10
[Mo]
(ppm)
0
200
400
δ15N
n=202
n=34
n=173
n=15
n=3
0
4
8

Table S1: FeT/Al ratios for Svalbard shales from the three units samples for nitrogen isotope analyses.

Sample	Stratigraphic unit	FeT/Al
G436.138	lower Dracoisen Fm	0.37
G436.120	lower Dracoisen Fm	0.51
G436.105	lower Dracoisen Fm	0.71
G436.101.5	lower Dracoisen Fm	0.42
G436.95.5	lower Dracoisen Fm	0.45
G436.88	lower Dracoisen Fm	0.42
G436.64	lower Dracoisen Fm	0.44
G436.42	lower Dracoisen Fm	0.40
G436.10.5	lower Dracoisen Fm	0.49
G435.79.5	MacDonaldryggen Mbr	0.61
G435.76	MacDonaldryggen Mbr	0.62
G435.66	MacDonaldryggen Mbr	0.57
G435.56	MacDonaldryggen Mbr	0.58
G435.45	MacDonaldryggen Mbr	0.55
G435.35	MacDonaldryggen Mbr	0.48
G435.25	MacDonaldryggen Mbr	0.43
G435.18	MacDonaldryggen Mbr	0.32
G521.46	lower Russøya Mbr	0.37
G521.44.4	lower Russøya Mbr	0.55
G521.40.5	lower Russøya Mbr	0.97
G521.36	lower Russøya Mbr	0.59
G521.33	lower Russøya Mbr	1.16
G521.30	lower Russøya Mbr	0.27
G521.26.4	lower Russøya Mbr	0.84
G521.23.4	lower Russøya Mbr	0.66
G521.19.6	lower Russøya Mbr	0.45
G521.18.9	lower Russøya Mbr	0.19
G521.13.2	lower Russøya Mbr	0.22
G521.6.2	lower Russøya Mbr	0.24
G521.3.7	lower Russøya Mbr	0.34
Detrital baseline		
G526f	Wilsonbreen Fm	0.55
G526j	Wilsonbreen Fm	0.61

Table S2: Comparison of nitrogen content and $\delta^{15}N$ results obtained for bulk and decarbonated samples, measured by either static or by conventional isotope ratio mass spectrometry.

Samples name	decarb [a] wt %	**Bulk samples**				**Decarbonated samples**				Average **$\delta^{15}N$ ‰**
		Static		Conventional		Static		Conventional		
		N_{bulk} ppm	**$\delta^{15}N$** ±0.3‰	N_{bulk} ppm	**$\delta^{15}N$** ±0.15‰	N_{bulk} ppm	**$\delta^{15}N$** ±0.3‰	N_{bulk} ppm	**$\delta^{15}N$** ±0.15‰	
TeS 46	93	60	**3.6**			63	**2.5**	71	**3.6**	**3.2±0.63**
TeS 30	80	97	**5.3**			81	**5.1**	81	**4.8**	**5.1±0.25**
CRS 16	60					301	**5.1**	300	**4.6**	**4.8±0.30**
δXM01	10	770	**4.1**					530	**3.3**	**3.7±0.55**
XM0107	11	945	**4.2**	970	**4.7**			980	**4.0**	**4.3±0.35**
do1008	93	70	**4.4**			61	**4.1**			**4.3±0.21**
do1013	59	685	**5.4**					630	**5.8**	**5.6±0.28**
HU 99	5	1664	**5.4**	1640	**4.9**			1550	**5.1**	**5.1±0.28**
HU 110	84	140	**5.6**					110	**5.7**	**5.7±0.07**
do0603	98	32	**3.5**			17	**4.0**			**3.8±0.35**
do0329	74	200	**4.1**					130	**4.4**	**4.2±0.21**
do0351	97	19	**3.4**			5	**3.1**			**3.3±0.21**
HU 180	89	140	**2.5**			101	**1.9**			**2.2±0.42**

[a] decarb: weight percent of the initial mass remaining after HCl attack

Table S3: $\delta^{15}N$, $\delta^{13}C_{carb}$, C_{org}, $\delta^{13}C_{org}$, N content and N/C results for late Neoproterozoic samples from Brazil, NW Canada, NE Svalbard and South China. $\delta^{13}C_{carb}$, $\delta^{13}C_{org}$ and C_{org} are from other studies for South China (Ader et al., 2009) and Brazil (Sansjofre et al., 2011; Sansjofre, 2011).

Formation	Stratigr. height (m)	Sample name	decarb (wt%)	$\delta^{15}N$ ± 0.1‰				[N] ppm decarb[1]			[N] ppm bulk[2]	Corg %		$\delta^{13}C_{carb}$ ± 0.1‰	$\delta^{13}C_{org}$ ± 0.1‰	C/N at
				1st	2nd	3rd	Avg	1st	2nd	Avg		decarb	Bulk			
Yangjiaping section, Yangtze platform, South China[3]																
Datangpo	-93	XM0101	54	4.3[Sb]							210 [Sb]	0.23	0.11	-5.2	-26.4	5.9
Datangpo	-92.5	XM0103	12	3.3[Sb]							1010 [Sb]	5.6	4.89		-31.7	56
Datangpo	-92	δXM01	10	4.1[Sb]	3.3[b]		**3.7**				770 [b]	3.0	2.69		-31.3	41
Datangpo	-91.5	XM0107	11	4.2[Sb]	4.7[b]	4.0	**4.3**	1100			945[Sb]	0.19	0.17		-29.0	2.1
Datangpo	-91	XM0109	9	4.6[b]							970[b]	0.13	0.12	-1.8	-26.2	1.4
Doushantuo	0.4	do1002		3.2[Sb]							70[Sb]			-4.3		
Doushantuo	0.7	do1004	94	3.8				1620			97*	4.4	0.26	-5.0	-30.0	32
Doushantuo	1.1	do1008	93	4.4[Sb]	4.1[S]		**4.3**	875[S]			70[Sb]	2.0	0.14	-4.5	-29.2	27
Doushantuo	3.3	do1013	59	5.4[Sb]	5.8		**5.6**	1540			685[Sb]	0.33	0.14	-4.9	-27.6	2.3
Doushantuo	3.8	do1015		5.3[Sb]							590[Sb]			-5.2		
Doushantuo	11.7	HU 99	5	5.4[Sb]	4.9[b]	5.1	**5.1**	1630			1664[Sb]	2.6	2.44		-32.1	17
Doushantuo	15.6	δdo 0406	6	5.8[b]							1110[b]	0.22	0.21		-29.1	2.2
Doushantuo	38.6	HU 106	52	5.6[Sb]							336[b]	0.49	0.24	2.3	-26.0	8.2
Doushantuo	0.7	HU 110	84	5.6[Sb]	5.7		**5.7**	700			140[Sb]	4.6	0.73	5.5	-25.1	61
Doushantuo	26.6	do 0603	98	3.5[Sb]	4.0[S]		**3.8**	983[S]			32[Sb]	9.6	0.17	7.7	-23.4	61
Doushantuo	52.9	HU 125	96	4.8[Sb]							60[Sb]	3.9	0.16	6.9	-21.1	31
Doushantuo	56.0	do 0625	97	3.2[S]				560[S]			15.9*	8.6	0.24	7.2	-22.4	179
Doushantuo	74.5	do 0635	98	4.0[S]				400[S]			9.5*	11.9	0.28	7.3	-20.9	346
Doushantuo	94.4	do 0301	75	5.2[Sb]							310[Sb]	2.5	0.61	5.7	-25.3	23
Doushantuo	115.9	do 0309	99	2.8				421			4,1*	2.2	0.02	4.1	-28.1	60
Doushantuo	131.0	do 0319	59	3.2[Sb]							510[Sb]	2.2	0.90	1.8	-26.9	20
Doushantuo	152.1	do 0329	74	4.1[Sb]	4.4		**4.3**	490			200[Sb]	1.7	0.44	2.2	-26.5	26
Dengying	183.3	do 0351	97	3.4[Sb]	3.1[S]		**3.3**	180[S]			19[Sb]	0.73	0.02	3.0	-24.0	12
Dengying	196.0	HU 180	89	2.5[Sb]	1.9[S]		**2.2**	950[S]			140[Sb]	7.7	0.83	-1.4	-29.5	69
Dengying	216.0	do1105	99.8	3.2[Sb]							20[Sb]	37	0.06	5.9	-27.3	36

Table S1 continued

Formation	Stratigr. height (m)	Sample name	decarb (%)	$\delta^{15}N$ ± 0.1‰				[N] ppm decarb[1]			[N] ppm bulk[2]	Corg %		$\delta^{13}C_{carb}$ ± 0.1‰	$\delta^{13}C_{org}$ ± 0.1‰	C/N at
				1st	2nd	3rd	Avg	1st	2nd	Avg		decarb	Bulk			
Terconi section, Brazil[4]																
Mirassol d'Oeste	4.2	TeS 5	99.5	4.4[S]				1073[S]			5*	38	0.18	-4.7		409
Mirassol d'Oeste	8.2	TeS 13	99.8	2.4[S]				788[S]			1*	24	0.05	-3.5	-27.7	352
Mirassol d'Oeste	9.2	TeS 15	95	10.0[S]				283[S]			14*	0.58	0.03	-3.5	-26.5	24
Mirassol d'Oeste	10.7	TeS 18	93	7.9				223			14*	0.88	0.06	-3.9	-26.8	51
Mirassol d'Oeste	11.7	TeS 20	93	6.0[S]				2391[S]			168*	9.0	0.63	-4	-27.9	44
Mirassol d'Oeste	12.7	TeS 22	92	4.6[S]	5.1[S]		**4.9**	1101[S]	1061[S]	**1081**	91*	6.2	0.52	-4.1	-27.8	66
Guia	15.7	TeS 28	89	6.0				286			32*	1.0	0.11	-5.1	-27.4	39
Guia	16.4	TeS 30	80	5.1[S]	4.8	5.3[Sb]	**5.1**	399[S]	444	**422**	97[Sb]	1.1	0.23	-5.1	-27.5	31
Guia	17.2	TeS 32	89	3.2				563			63*	1.3	0.15	-5.2	-27.6	27
Guia	21.7	TeS 40	92	4.0	4.1		**4.0**	875	637		71*	1.1	0.09	-5.1	-27.5	15
Guia	27.2	TeS 42	85	5.4				504			75*	0.34	0.05	-5.2	-27.7	7.8
Guia	28.2	TeS 44	88	4.3	5.1		**4.7**	532	636	**584**	73*	0.64	0.08	-5	-27.5	13
Guia	30.7	TeS 46	93	2.5[S]	3.6	3.6 [Sb]	**3.2**	889[S]	1072	**980**	60[Sb]	1.8	0.13	-4.8	-27.9	22
Mirassol d'Oeste	12.8	TR+2.80	93	6.9				287			20*	2.1	0.15	-4.9	-27.9	86
Mirassol d'Oeste	10.6	TR +0.60	91	6.8	6.8		**6.8**	406	249	**328**	30*	1.7	0.15	-8.8	-27.6	60
Mirassol d'Oeste	10.2	TR +0.20	91	6.1				388			35*	4.2	0.38	-9.5	-27.9	125
Mirassol d'Oeste	10	TR -0.3	93	10.2	10.8		**10.5**	126	125	**126**	9*	0.41	0.03	-4.1	-27.6	38
Mirassol d'Oeste	8.3	TR-1.7	96	6.2	6.9		**6.5**	772	710	**741**	30*	5.7	0.23	-4.1	-27.9	90
Mirassol d'Oeste	7.3	TR-2.7	98	8.6				345			7*	17	0.34	-3.9	-27.5	575
Camil section, Brazil[4]																
Guia	112.7	CAS 1	90	3.7				181			18*	0.69	0.07	-1.8	-31.8	45
Guia	111.7	CAS 2	90	3.9				267			27*			-2.0		
Carmelo section, Brazil[4]																
Guia	57.6	CRS 0	31	4.4				155			108	0.07	0.05	-5.3	-26.5	5.1
Guia	82.9	CRS 2n	24	4.4	4.0	3.7	**4.0**	260	270	**265**	201	0.12	0.09	-5.1	-27.5	5.5
Guia	84.8	CRS 3	63	3.4				203			75	0.11	0.04	-4.9	-28.5	6.1
Guia	85.6	CRS 4	20	3.2				278			224	0.12	0.10	-4.5	-31.8	5.0
Guia	107.3	CRS 5	64	4.2	3.9		**4.1**	284	299	**292**	108	0.29	0.10	-4.1	-31.9	11

Table S1 continued

Formation	Stratigr. height (m)	Sample name	decarb (%)	$\delta^{15}N$ ± 0.1‰				[N] ppm decarb[1]			[N] ppm bulk[2]	Corg %		$\delta^{13}C_{carb}$ ± 0.1‰	$\delta^{13}C_{org}$ ± 0.1‰	C/N at
				1st	2nd	3rd	Avg	1st	2nd	Avg		decarb	Bulk			
Guia	110.8	CRS 7	69	5.5				97			30	0.09	0.03	-3.9	-31.0	10
Guia	111.6	CRS 8	98	4.6[S]				149[S]			4*	0.36	0.01	0.0	-28.2	28
Guia	120.6	CRS 11	97	3.9				390			10*	0.53	0.01	-3.1	-31.0	16
Guia	140.1	CRS 13	81	4.2	3.6		**3.9**	203	196	**199**	38	0.19	0.04	-2.0	-30.1	11
Guia	159.2	CRS 16	60	5.1[S]	4.7		**4.9**	336[S]	301	**319**	134	0.46	0.18	-2.0	-32.0	16
Guia	167.1	CRS 19	96	2.6				410			16*	0.67	0.03	-0.7	-30.4	19
Guia	170.6	CRS 20	98	2.7				1264			21*	3.7	0.06	-1.0	-31.2	34
Guia	178.6	CRS 23	93					151			10*	0.63	0.04	-0.5	-30.8	48
Guia	181.2	CRS 24	83	5.1				369			68	0.96	0.16	-0.5	-32.1	28
Guia	191.8	CRS 28	96					124			5*	0.22	0.01	-0.3	-28.2	21
Guia	197.1	CRS 30	20	5.8[S]				380[S]			304	0.76	0.60	-0.9	-31.8	23
Guia	201.3	CRS 32	76	5.4				145			35	0.21	0.05	-0.3	-29.9	17
Guia	207.7	CRS 35	90					98			10*	0.14	0.01	-0.0	-28.7	16
Copacel section, Araras platform, Brazil[4]																
Guia	35.1	NOS 13	98	4.8				425			7*	0.57	0.01	-0.2	-28.1	16
Guia	76.2	NOS 8	68					101			32	0.09	0.03	-3.9	-29.7	10
Guia	201.3	CP 1	89	2.3				146				0.32	0.03	-1.0	-30.8	
Guia	259.3	CP13	95	2.2				1009			48*	2.1	0.10	-0.8	-31.2	24
Guia	333.8	CP 51	75	5.0				545			138	1.5	0.38	-3.0	-32.6	32
Northeast Svalbard composite section[5]																
Dracoisen	19.4	G136-19.4		4.1				540	580	**560**		0.54			-33.9	11
Dracoisen	24.1	G136-24.1		4.7	4.5		**4.6**	490	490	**490**		0.57			-34.1	14
Dracoisen	105	G436-105		5.2				700								
Dracoisen	88	G436-88		5.2				720				0.28			-31.2	4.5
Dracoisen	64	G436-64		5.6				600				0.99			-34.9	19
Dracoisen	42	G436-42		4.3				390				0.29			-32.6	8.7
Dracoisen	159	G306-159		5.3				1080								
Dracoisen	143	G306-143		5.8				700				1.26				

Table S1 continued

Formation	Stratigr. height (m)	Sample name	decarb (%)	$\delta^{15}N$ ± 0.1‰				[N] ppm decarb[1]			[N] ppm bulk[2]	Corg %		$\delta^{13}C_{carb}$ ± 0.1‰	$\delta^{13}C_{org}$ ± 0.1‰	C/N at
				1st	2nd	3rd	Avg	1st	2nd	Avg		decarb	Bulk			
Macdonaldryggen	-25	G435-25		6.3				320				0.31			-30.4	11
Macdonaldryggen	-35	G435-35		4.2												
Macdonaldryggen	-56	G435-56		4.8				670				0.55			-32.7	9.6
Macdonaldryggen	-66	G435-66		5.5				680				0.68			-32.6	12
Macdonaldryggen	-76	G435-76		4.6				680								
Macdonaldryggen	-79.5	G435-79.5		5.5	5.3		**5.4**	610	590	**600**		0.64			-32.4	12
Russøya Mb.	114	G406-35		4.2	4.5		**4.4**	1280	1240	**1260**		0.42				
Russøya Mb.	106.5	G406-42		4.2				450				6.56			-27.9	170
Russøya Mb.	43.5	P5014-43.5		4.7				630								
Northwest Canada composite section[6]																
Sheepbed	94	G4-94		2.6				1060				1.13			-30.8	11
Sheepbed	73	G4-93		3.7				590				0.62			-30.3	10
Sheepbed	36	G4-36		3.3				680				0.33			-29.4	4.9
Sheepbed	8	G4-8		3.1				650				0.35			-31.3	5.4
Twitya	163	F849.163		3.5[b]							1030[b]					
Twitya	135	F849.135		2.4[b]							930[b]					
Twitya	87	F849.87		2.5[b]							650[b]					
Twitya	46	F849.46		2.1[b]							510[b]					

Most N content and $\delta^{15}N$ measurements were performed on decarbonated samples by conventional mass spectrometry. N content and $\delta^{15}N$ measurements performed on bulk samples are indicated by [b] and measurements performed using the static mass spectrometry are indicated by [S].

[1] [N] ppm decarb: values correspond to the direct measurement of the nitrogen content in the decarbonated residu.

[2] [N] ppm bulk : values correspond either to direct measurement of the nitrogen content in bulk samples or in the recalculated nitrogen content in the bulk samples from the nitrogen content in the decarbonated residu and the mass pourcent of mass loss after decarbonatation (decarb %).

* indicates most probably underestimated N content in bulk rocks, owing to possible mass loss during the decarbonatation procedure (see method section in the main text and Table S2)

[3] For the South China data, the 0 datum correspond to the contact between the cap carbonate and the Nantuo Diamictite.

[4] For the Brazilian data, the datums are as follows, 0 = contact with the Marinoan Diamictites of the Puga Formation for Terconi, Carmelo and Copacel sections. For Camil section, 0 = firt outcrop of the Guia Formation observed in Camil quarry, which is 114 m below the Guia-Serra Do Quilombo transition.

[5] For the Svalbard data, the datums are as follows: for the Dracoisen formation, 0 = based of the formation; for the Macdonaldryggen Member, 0 = the top of the member; for the Russøya Member, 0 = the base of the member

[6] For the NW Canada data, the 0 m datums are the base of each formation.